JGR Solid Earth

RESEARCH ARTICLE
10.1029/2025JB032410

Wedge Inelasticity and Fully Coupled Models of Dynamic Rupture, Ocean Acoustic Waves, and Tsunami in the Japan Trench: The 1896 Sanriku Earthquake

Yue Du[1,2] **and Shuo Ma**[1]

[1]Department of Earth and Environmental Sciences, San Diego State University, San Diego, CA, USA, [2]Scripps Institution of Oceanography, University of California, San Diego, CA, USA

Key Points:

- Inelastic wedge deformation accounts for large tsunamigenesis and depletion in high-frequency radiation in the 1896 Sanriku earthquake
- Plastic dissipation in the wedge leads to ~10 times lower moment-scaled radiated energy than regular earthquakes
- Ocean acoustic waves may not provide robust signals for tsunami early warning

Supporting Information:

Supporting Information may be found in the online version of this article.

Correspondence to:

S. Ma,
sma@sdsu.edu

Citation:

Du, Y., & Ma, S. (2025). Wedge inelasticity and fully coupled models of dynamic rupture, ocean acoustic waves, and tsunami in the Japan Trench: The 1896 Sanriku earthquake. *Journal of Geophysical Research: Solid Earth*, *130*, e2025JB032410. https://doi.org/10.1029/2025JB032410

Received 15 JUL 2025
Accepted 28 SEP 2025

Author Contributions:

Conceptualization: Yue Du, Shuo Ma
Data curation: Yue Du, Shuo Ma
Formal analysis: Yue Du, Shuo Ma
Funding acquisition: Shuo Ma
Investigation: Yue Du, Shuo Ma
Methodology: Yue Du, Shuo Ma
Project administration: Shuo Ma
Resources: Yue Du, Shuo Ma
Software: Yue Du, Shuo Ma
Supervision: Shuo Ma
Validation: Yue Du, Shuo Ma
Visualization: Yue Du, Shuo Ma
Writing – original draft: Yue Du
Writing – review & editing: Shuo Ma

Abstract One of the essential characteristics of earthquakes associated with large tsunami generation is the depletion of high-frequency radiation, which is not well understood by elastic dislocation theory and largely not accounted for in most rupture models of real events. We present fully coupled models of dynamic rupture, ocean acoustic waves, and tsunami for the 1896 Sanriku earthquake with wedge inelasticity. The inelastic wedge deformation due to thick sediment in the northern Japan Trench is shown to generate efficient short-wavelength seafloor uplift (>5 m), which is several times larger than the uplift by elastic dislocation models and generates impulsive tsunami that can have a large impact on the rugged Sanriku coast. Seismic moment due to inelastic wedge deformation has a reverse faulting focal mechanism with a steep plunge (>75°) of T axis, reflecting high efficiency in tsunami generation. However, the inelastic deformation is a large energy sink, which causes slower rupture velocity, weaker radiation of ocean acoustic and seismic waves, and ~10 times lower moment-scaled radiated energy than those of elastic models, explaining nearly all the anomalous characteristics of this tsunami earthquake. The anti-plane off-fault shear stress in the mode III rupture direction, limited by yielding, plays an important role in the slow rupture velocity and energy radiation along strike. Ocean acoustic waves may not provide robust signals for tsunami early warning due to weak high-frequency radiation. Additionally, large, long-duration ground velocity pulses can naturally result from inelastic deformation.

Plain Language Summary The 1896 Sanriku earthquake was one of the deadliest earthquakes in recorded Japanese history, well known for its anomalously large tsunami but weak ground shaking. It was classified as a tsunami earthquake. Similar anomalous characteristics were also observed in the northern Japan Trench in the 2011 M_W 9.1 Tohoku-Oki earthquake. The physics of large tsunamigenesis and weak ground shaking remains poorly understood. We explain these anomalous characteristics of the 1896 Sanriku earthquake by inelastic wedge deformation in fully coupled models of dynamic rupture, ocean acoustic waves, and tsunami. Inelastic deformation of thick wedge sediment in the northern Japan Trench is shown in the models to produce efficient short-wavelength tsunami with small shallow slip, slow rupture velocity, depletion in high-frequency radiation, and low moment-scaled radiated energy, accounting for nearly all the anomalous characteristics of this earthquake. Ocean acoustic waves may not provide robust early warning signals for tsunami. The physics shown in this work can have important implications for tsunami early warning and hazard assessment around the world.

1. Introduction

The 1896 Sanriku earthquake was one of the two tsunami earthquakes identified by Kanamori (1972). The earthquake was only weakly felt, but the tsunami that arrived ~30 min later devastated coastal towns along the Sanriku coast, killing more than ~22,000 people (Shuto et al., 2007). The death toll surpassed that of the 2011 M_W 9.1 Tohoku-Oki earthquake, making it one of the deadliest earthquakes in recorded Japanese history. The surface wave magnitude was M_S 7.2 (Abe, 1978) estimated from global data, well below the moment magnitude ~M_W 8.0 (Utsu, 1994), reflecting the deficiency in high-frequency radiation. The seismic intensity was only 2–3 on the Japan Meteorological Agency (JMA) scale and 4–5 on the Modified Mercalli scale (e.g., Satake et al., 2017). However, the largest tsunami runup reached up to 40 m (Iki, 1897; Matsuo, 1933), similar to that of the M_W 9.1 Tohoku-Oki earthquake despite the lower magnitude.

Over the last 50 years, tens of other tsunami earthquakes have been identified from better-quality data (e.g., Felix et al., 2021; Lay et al., 2012). However, the 1896 Sanriku earthquake remains one of the most anomalous events,

and the physics of the deficiency in high-frequency radiation and large tsunamigenesis is elusive. The earthquake occurred in the northern Japan Trench, with epicenter at (144°E, 39.5°N) (Utsu, 1979), which is the same region that generated a devastating tsunami in the 2011 Tohoku-Oki earthquake that caused extreme runup along the Sanriku coast, more than 100 km north of the epicenter.

Only a few studies modeled this earthquake, mostly using tsunami data. Kanamori and Kikuchi (1993) suggested a large submarine landslide for the tsunami source due to the puzzling depletion in high-frequency radiation. Tanioka and Satake (1996) and Tanioka and Seno (2001) presented simple elastic dislocation models with uniform slip. They found that a rupture zone of about 200 km long along strike and less than 50 km wide located close to the trench, is required by the tsunami data. Tanioka and Seno (2001) also proposed simple conceptual models of inelastic deformation, showing that with inelastic deformation tsunami data can be explained by smaller fault slip than elastic dislocation models. Satake et al. (2017) inverted waveform data at 3 tidal gauges in the far field using eight subfaults of Satake et al. (2013) for the 2011 Tohoku-Oki earthquake in the northern Japan Trench and concluded that the 1896 earthquake occurred deeper than the northern rupture of the 2011 Tohoku-Oki earthquake. Ma and Nie (2019) rigorously incorporated inelastic wedge deformation in a dynamic rupture model for a generic M_W 8.0 earthquake similar to the 1896 Sanriku earthquake and suggested that inelastic wedge deformation of thick sediment in the northern Japan Trench (Kodaira et al., 2017; Tsuru et al., 2002) can explain the large tsunamigenesis with small shallow slip and weak high-frequency radiation. Du et al. (2021) modeled the 1896 Sanriku tsunami by solving a nonlinear Boussinesq equation using an inelastic wedge deformation model of Ma and Nie (2019) and produced tsunami runup in good agreement with the observations (Iki, 1897; Matsuo, 1933), better than those of Satake et al. (2017) obtained from an inversion. They emphasized the importance of short-wavelength inelastic uplift in generating impulsive tsunamis that can have large impacts on the rugged Sanriku coast. Both models of Ma and Nie (2019) and Du et al. (2021) did not fully address the seismic and ocean acoustic radiations due to inelastic deformation, which is the goal of this work.

In Ma and Du (2025), we presented fully coupled models of dynamic rupture, ocean acoustic waves, and tsunami for the 2011 M_W 9.1 Tohoku-Oki earthquake based on the dynamic rupture models of Ma (2023). The models are not an update of Ma (2023) because both models are nearly identical, but instead focused more on the radiation of ocean acoustic and seismic waves allowed by the fully coupled approach. The models showed that inelastic wedge deformation in the northern Japan Trench produces large seafloor uplift (~4 m) with shallow slip <20 m, consistent with the differential bathymetry observations (Fujiwara, 2021; Fujiwara et al., 2017; Kodaira et al., 2021) and gives rise to slow rupture propagation (~850 m/s) and reduced radiation of ocean acoustic and seismic waves. The slow rupture propagation and weak high-frequency radiation are largely due to plastic dissipation in the wedge (Ma & Hirakawa, 2013). However, the frictional sliding on microfractures with steep dips, mimicked by inelastic deformation, generates tsunami more efficiently than slip on a shallowly dipping plate interface (Ma, 2012). The dynamic rupture model with inelastic wedge deformation in the northern Japan Trench provided a more consistent explanation for the various observations of differential bathymetry, turbidites, tsunami, and energy radiation of this earthquake than all the elastic dislocation models to date.

In this work, we use the same modeling approach of Ma and Du (2025) and present fully coupled models of dynamic rupture, ocean acoustic waves, and tsunami for the 1896 Sanriku earthquake. The models will be focused on the northern Japan Trench only due to a smaller rupture extent. We will show that inelastic wedge deformation can account for nearly all the anomalous characteristics of this tsunami earthquake mentioned earlier. The models, however, are not intended to represent detailed rupture process of the earthquake due to limited observations available. Furthermore, the inelastic wedge deformation will be shown to represent a reverse faulting focal mechanism with a steep plunge (>75°) of T axis, reflecting high efficiency in tsunami generation. The additional radiation from the moment tensors in the wedge provides a new way of testing different hypotheses for tsunami generation (e.g., shallow slip, submarine landslide, or inelastic wedge deformation).

2. Fully Coupled Models

As in Ma and Du (2025), we use the fault geometry, bathymetry, and velocity structure from the Japan Integrated Velocity Structural Model (JIVSM) based on Koketsu et al. (2012) and incorporate the sediment thickness variation along the Japan Trench from Tsuru et al. (2002). The P- and S-wave speeds and density in the sedimentary wedge are 3,000 m/s, 1,500 m/s, and 2,250 kg/m^3, respectively. In the Tohoku-Oki earthquake models by Ma (2023) and Ma and Du (2025), a 10° dipping fault segment was added between the trench and the plate

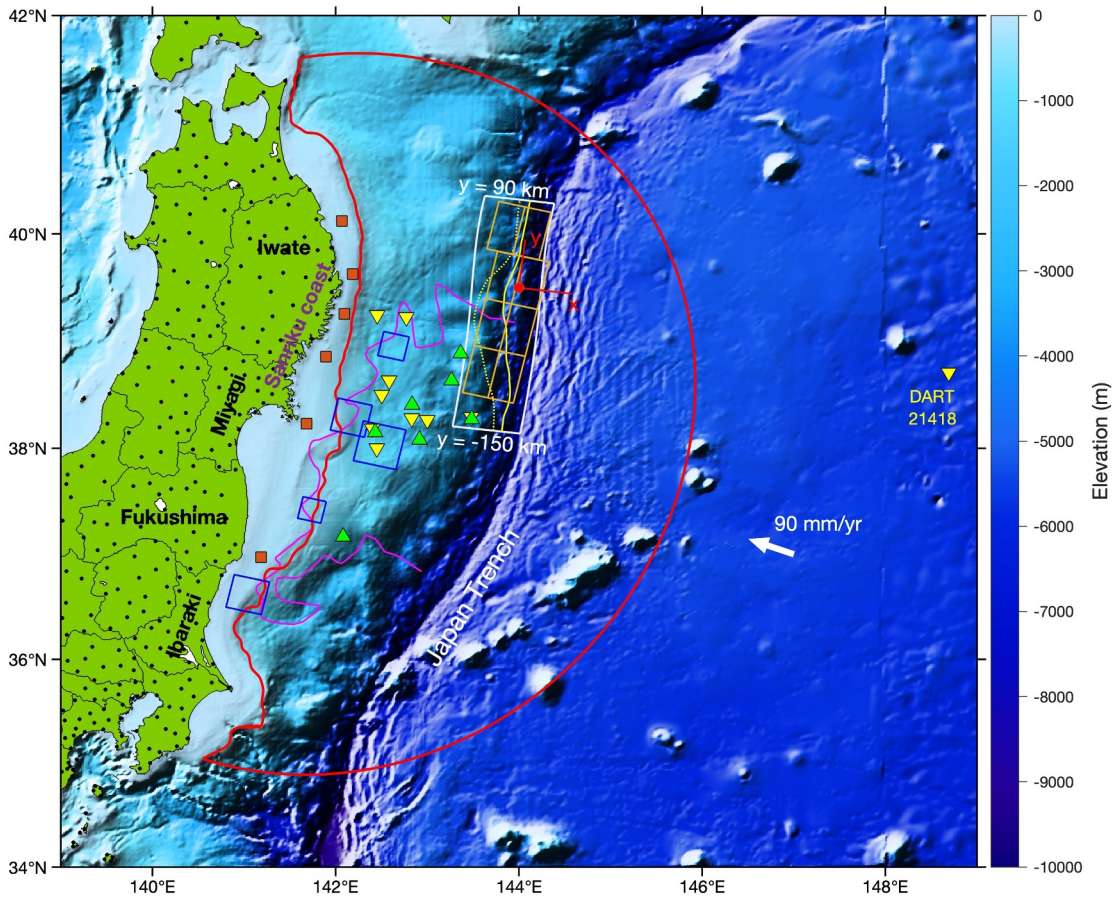

Figure 1. Map of the study. The white box denotes the fault used in this work. The eight yellow rectangles are the subfaults used to model the 1896 Sanriku earthquake in Satake et al. (2017). The yellow solid and dotted lines denote the traces of the backstop surface on the seafloor and plate interface, respectively, by fitting the sediment thickness data of Tsuru et al. (2002). Thick sediment in the northern Japan Trench is seen. The 1896 epicenter (144°E, 39.5°) is denoted as a red dot, which is the origin of the coordinate system in this work (*x* is along E5°S and *y* N5°E, shown in red). The red crescent-shaped curve outlines the ocean of interest in this work. The stations that recorded the 2011 Tohoku-Oki earthquake and tsunami used in Ma (2023) are shown as a reference: seafloor GPS stations (green triangles), ocean bottom pressure sensors (yellow inverted triangles), GPS buoys (orange squares), and on-land GPS stations (black dots); the data sources were given in Kubota et al. (2022). Also shown are the models of strong motion generation areas (blue squares) and coseismic rupture extent (magenta curve) of the 2011 Tohoku-Oki earthquake; the data sources were given in Ma (2023). These features are identical to those in Figure 1 of Ma and Du (2025).

interface, allowing the rupture to reach the trench, as the plate interface in the JIVSM does not extend to the seafloor. In this work, we exclude this dipping fault segment and consider buried rupture only for simplicity, because this fault segment appears artificial in the narrow rupture zone of the Sanriku earthquake model. The top of the fault is only about <1 km below the trench based on the JIVSM (see Figure 5). We consider a fault 240 km along strike and 65 km along dip to include the entire sedimentary wedge (Figure 1). The actual rupture zone of the model is less than 40 km wide and ~200 km long controlled by the fault frictional parameters (shown in Figure 2). The fault covers largely the same area considered in Satake et al. (2017); they used an 8° dipping planar plate interface, nearly twice as large as the actual fault dip. We add the ocean in the same way as in Ma and Du (2025), which spans the same spatial extent (Figure 1). The coordinate system used in this work is shown in Figure 1: *x* is approximately perpendicular to the trench (along E5°S), *y* along N5°E, and the origin is at the epicenter (144°E, 39.5°N).

To fully couple the ocean and the seafloor we enforce the continuity of normal traction and normal velocity and displacement and vanishing shear traction on the seafloor. The traction-at-split-node scheme is used on the seafloor as well as on the fault. The linearized sea surface boundary condition of Lotto and Dunham (2015), verified by Wilson and Ma (2021) in a semi-analytical solution, is used on the sea surface, which naturally simulates the ocean acoustic waves and tsunami with dispersion. The boundary conditions at the seafloor (also linearized) account for tsunami generation by horizontal displacement (Tanioka & Satake, 1996) with variable

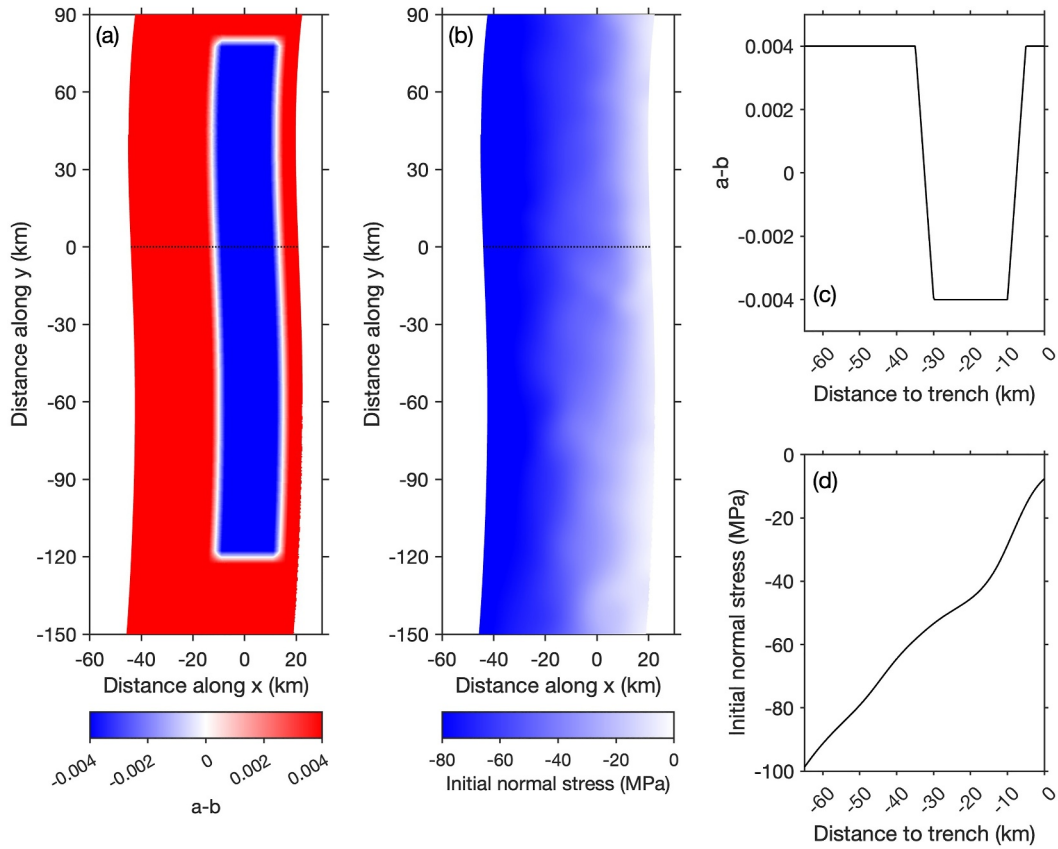

Figure 2. Distributions of $a - b$ (a) and initial normal stress (b) are mapped on the fault and a cross section of (a) and (b) along $y = 0$ is shown in (c) and (d), respectively.

ocean depths. We refer the reader to Ma and Du (2025) and references therein for more detailed descriptions of the fully coupled approach. The 3D finite-element code used in this work as well as in Ma (2022) and Ma and Du (2025) participates in the Cascadia Region Earthquake Science Center (CRESCENT) benchmark exercises for fully-coupled earthquake-tsunami simulations (Kutschera et al., 2025).

To set up the initial fault stress and stress and pore pressure in the sedimentary wedge, we use the 3D critical wedge solution derived in Ma (2023), which gives rise to stresses in the wedge as well as on the fault when the maximum compressive stress is at an oblique angle to the wedge strike. The solution is an extension of the 2D critical wedge solution of Dahlen (1984), which assumed that the maximum compressive stress is normal to the wedge. In Ma (2023) and Ma and Du (2025), the fault stress from the critical solution was abandoned and the fault stress derived from the heterogeneous stress drop model of Kubota et al. (2022) was used to explain the observations. Such a stress drop model for the 1896 Sanriku earthquake is unavailable due to limited observations. We choose to use the fault stress from the critical solution for simplicity, as in Ma and Nie (2019), which is consistent with the stress and pore pressure conditions in the wedge. Future work can incorporate more heterogeneities in the model. The surface slope and fault dip are obtained by fitting the data in the northern Japan Trench in the finite element mesh (Figure S1 in Supporting Information S1), which are 5.475° and 4.7313°, respectively. The maximum compressive direction is assumed along the plate convergence direction, E20°S, and makes an inclination angle of 8° from the wedge slope. The rake of initial shear stress on the fault is assumed to be 87°. Assuming the frictional coefficient at the base of the wedge is 0.25, the 3D critical wedge solution directly gives the pore pressure ratio 0.5856 (slightly overpressured; see equation 6 in Dahlen, 1984) and internal friction 0.3261. The details in the 3D critical solution can be seen in the Appendix of Ma (2023). The inclination angle used here is smaller than the 15° used in Ma (2023) because this angle largely controls the fluid pressure in the wedge. Larger angles lead to larger fluid overpressure, giving rise to too small of stress drop for the modeling of the 1896 Sanriku earthquake.

The rake angle is an important parameter in our models as it controls the amplitudes of on-fault shear stresses along the strike and dip. The chosen rake angle due to oblique plate convergence leads to a small left-lateral strike-slip component. If we define x' as the direction along dip (positive updip), y' along strike (positive north), and z' perpendicular to the fault plane (positive up; see Figure A1 in Ma, 2023), the shear stress $\sigma_{z'y'}$ determines the off-fault shear stress $\sigma_{y'x'}$ in the critical solution, which can play an important role in mode III ruptures (Andrews, 1976, 2004). The rupture propagation in the Sanriku earthquake is mostly along strike (mode III rupture). Along $+y'$ (north) large dynamic shear stress carried by the rupture front reduces the amplitude of $\sigma_{y'x'}$, while along $-y'$ (south) the amplitude of $\sigma_{y'x'}$ is increased by the rupture front. In mode III ruptures the change in the off-fault shear stress $\sigma_{y'x'}$ is directly proportional to slip velocity and if this stress is limited by yielding it has the effect of limiting slip velocity (Andrews, 1976, 2004). In model III, only stress components $\sigma_{y'x'}$ and $\sigma_{z'x'}$ are important in controlling yielding because other stress components do not change. Thus, the inelastic yielding will only occur in $-y'$ direction for a pure mode III rupture because of the increase of $\sigma_{y'x'}$ amplitude by rupture front, while along $+y'$ direction rupture front moves the material away from yielding by reducing the $\sigma_{y'x'}$ amplitude. Inelastic yielding contributes to fracture energy in controlling rupture velocity (Andrews, 2005). So, the rupture and slip velocities only to the south of the hypocenter are limited by yielding, while to the north they are similar to those of an elastic model (unaffected by the off-fault shear stress $\sigma_{y'x'}$). If we decrease the rake angle the amplitude of initial $\sigma_{y'x'}$ is larger; southward rupture propagation will be limited to a shorter extent while northward rupture is unaffected by yielding. If the rake angle is 90° (on-fault shear stress is along x' only) rupture and slip velocities cannot be controlled by yielding in the mode III direction, as in Ma and Nie (2019). Yielding still occurs at shallow depths due to mixed-mode rupture but does not control rupture velocity at depth. These important points will be shown in the results below.

Similar to Ma and Du (2025), we consider both elastic and inelastic models for the 1896 Sanriku earthquake. For the inelastic models, we use the Drucker-Prager yield criterion (Drucker & Prager, 1952), as in previous inelastic wedge deformation models (e.g., Ma & Nie, 2019). The yielding is assumed in shear only (e.g., Andrews, 2005), that is, there is no inelastic volumetric strain (compaction or dilatancy). In the undrained condition, dilatancy reduces pore pressure and strengthens the material thus decreasing the effect of yielding, while compaction increases pore pressure and weakens the material enhancing yielding, both of which were modeled for fault gouge (e.g., Hirakawa & Ma, 2016). However, the mechanical data for wedge sediment in high strain rates is limited, the assumption of yielding only in shear is a simple choice and serves as a starting point for building better inelastic wedge deformation models for tsunami generation in the future. No inelastic volumetric strain leads to moment tensors without isotropic component in the wedge, as we will show. We use the Biot's coefficient 0.5 and Skempton's coefficient 0.6 as in previous inelastic wedge deformation models, which are modest values for sedimentary rocks, to incorporate the effect of undrained pore pressure change on yielding during dynamic rupture.

The 3D critical wedge solution gives initial stresses, pore pressure, and internal friction in the wedge. To determine cohesion, we define a closeness-to-failure parameter (CF), which is the ratio of the square root of the second invariant of the deviatoric stress tensor to the yield stress (see Equation 9 in Ma, 2023). Because of a lack of data on material strength we use CF as a single free parameter to control the extent of yielding. Due to thick sediment in the northern Japan Trench, we set CF to be 0.9 (mimicking low cohesion of sediment so failure can occur easily) for $y \geq -60$ km, which covers most of the rupture zone (see Figure 4). We then allow CF to decrease smoothly as a cosine function from 0.9 to 0.7 for -120 km $\leq y < -60$ km (the functional form can be seen in equation 10 in Ma, 2023) and CF stays 0.7 for $y < -120$ km. The lower CF for $y < -60$ km near the southern end of rupture zone is to allow rupture to propagate more southward as southward rupture is significantly limited by the mode III yielding at depth (to be shown below), which has only a minor effect on the overall rupture characteristics. The CF value directly gives wedge cohesion as all the other parameters in the yield criterion are given by the critical wedge solution.

We use the rate-and-state friction with slip law for state evolution (see equations 1–6 in Ma, 2023) and standard frictional parameters to model dynamic rupture. Figure 2 shows the distributions of $a - b$ and the initial normal stress on the fault. The parameter b and state evolution distance L are 0.014 and 0.6 m everywhere on the fault. We confine the rupture zone to less than 40 km wide, similar to that in the northern Japan Trench in Ma (2023), by increasing $a - b$ linearly from -0.004 to 0.004 from 30 to 35 km from the trench. The rupture will penetrate the

deep velocity-strengthening region to a certain extent. At shallow depths, we also include a velocity-strengthening region, where $a - b$ increases linearly from −0.004 to 0.004 from 10 to 5 km from the trench. The velocity-strengthening region is also placed on the northern and southern ends of the rupture zone, to confine the rupture length to ∼200 km. Although constant wedge slope and fault dip are used in the 3D critical wedge solution, the fault and slope are slightly nonplanar, which results in a small variation of initial normal stress on the fault, but the normal stress increases approximately linearly with depth. The initial frictional coefficient on the fault also fluctuates slightly around 0.25, the value used in the critical solution. In Ma (2023), the velocity-weakening region extended to the trench in the northern Japan Trench as the stress drop model of Kubota et al. (2022) showed positive stress drop at shallow depths. Here we consider a velocity-strengthening region at shallow depths, as expected from shallow subduction zones (e.g., Scholz, 1998). The results for a shallow velocity-weakening zone will also be shown. The narrow shallow velocity-strengthening region (∼5 km wide) is due to the overall narrow rupture zone. The other frictional parameters are identical to those in Ma (2023) and Ma and Du (2025).

We nucleate the rupture by applying a 2D Gaussian perturbation in shear stress over 1 s on the fault (the standard deviation and peak amplitude of the Gaussian function are 2,500 m and 15% of the background shear stress, respectively) centered on the hypocenter. The hypocentral depth is 10.16 km based on the JIVSM. Due to the uncertainty in the hypocentral location of the 1896 earthquake we also consider two other hypocenters for the models, located at (0, −60 km) and (0, 60 km) with hypocentral depths of 9.96 and 10.36 km, respectively.

Due to a smaller rupture zone than in Ma and Du (2025), we discretize the sedimentary wedge using 250 m 4-node tetrahedral elements compared to 500 m in Ma and Du (2025), resulting in the element size on the fault of ∼250 m. The ocean is meshed using 500 m tetrahedral elements as in Ma and Du (2025), which can simulate ocean acoustic waves longer than ∼3 s accurately. The mesh gradually coarsens to a remote boundary, so reflected waves from the boundary do not contaminate the results. Each model is run for 300 s with a time step of 0.01 s.

3. Results

We show snapshots of slip velocity, shear stress change, vertical seafloor velocity, dynamic ocean bottom pressure (OBP) change, and sea surface elevation for the fully coupled elastic and inelastic models in Figures 3 and 4, respectively. The dynamic OBP change in this work as well as in Ma and Du (2025) is due to ocean acoustic waves and tsunami, that is, excluding the hydrostatic pressure change due to the seafloor displacement (see the second term on the right-hand side of equation A26 in Wilson & Ma, 2021). The detailed rupture processes of both models and the development of inelastic strain in the sedimentary wedge in the inelastic model are more clearly illustrated in Movies S1 and S2. After nucleation the rupture propagates in all directions with a faster rupture velocity along dip (mode II) than along strike (mode III). As the hypocenter is only ∼20 km down dip from the trench, the rupture reaches the trench at ∼14 s, exciting PL waves propagating landward (e.g., Kozdon & Dunham, 2014) and oceanic Rayleigh waves into the deep ocean. Large inelastic deformation occurs as the rupture propagates up dip from the hypocenter into the shallow velocity-strengthening region in the inelastic model, generating much larger seafloor uplift than the elastic model. The increase of shear stress on the fault due to the velocity-strengthening friction promotes inelastic failure in the wedge enhancing uplift, while in the elastic model the velocity-strengthening friction decreases slip and thus uplift. Ocean acoustic waves from down-dip rupture from the hypocenter are the first waves propagating landward. The down-dip rupture soon dies out in the deep velocity-strengthening region. The rupture in both models is seen to propagate predominantly along strike thereafter. Although the shear stress changes prescribed in both models are the same the two models are distinctly different. In the elastic model, the rupture propagates with a fast rupture velocity and large slip velocity (>5 m/s). The rupture front is seen as narrow pulses, generating strong waves trapped within the sedimentary wedge behind the rupture front. Large PL and oceanic Rayleigh waves are seen to radiate from the trapped energy behind the rupture fronts in both along-strike directions. In contrast, little radiation from the rupture fronts in the inelastic model is seen. The rupture velocity and slip velocity are much smaller. The excitation of ocean acoustic waves and trapped energy behind the rupture front are much weaker. However, the tsunami from the inelastic model is several times larger than that from the elastic model.

We observe a faster rupture velocity and shallower inelastic deformation zone to the north than to the south in the inelastic model. This is the role of off-fault shear stress $\sigma_{y'x'}$ in controlling the yielding for the mode III rupture, mentioned earlier. To the north, the dynamic shear stress associated with the rupture front decreases the amplitude

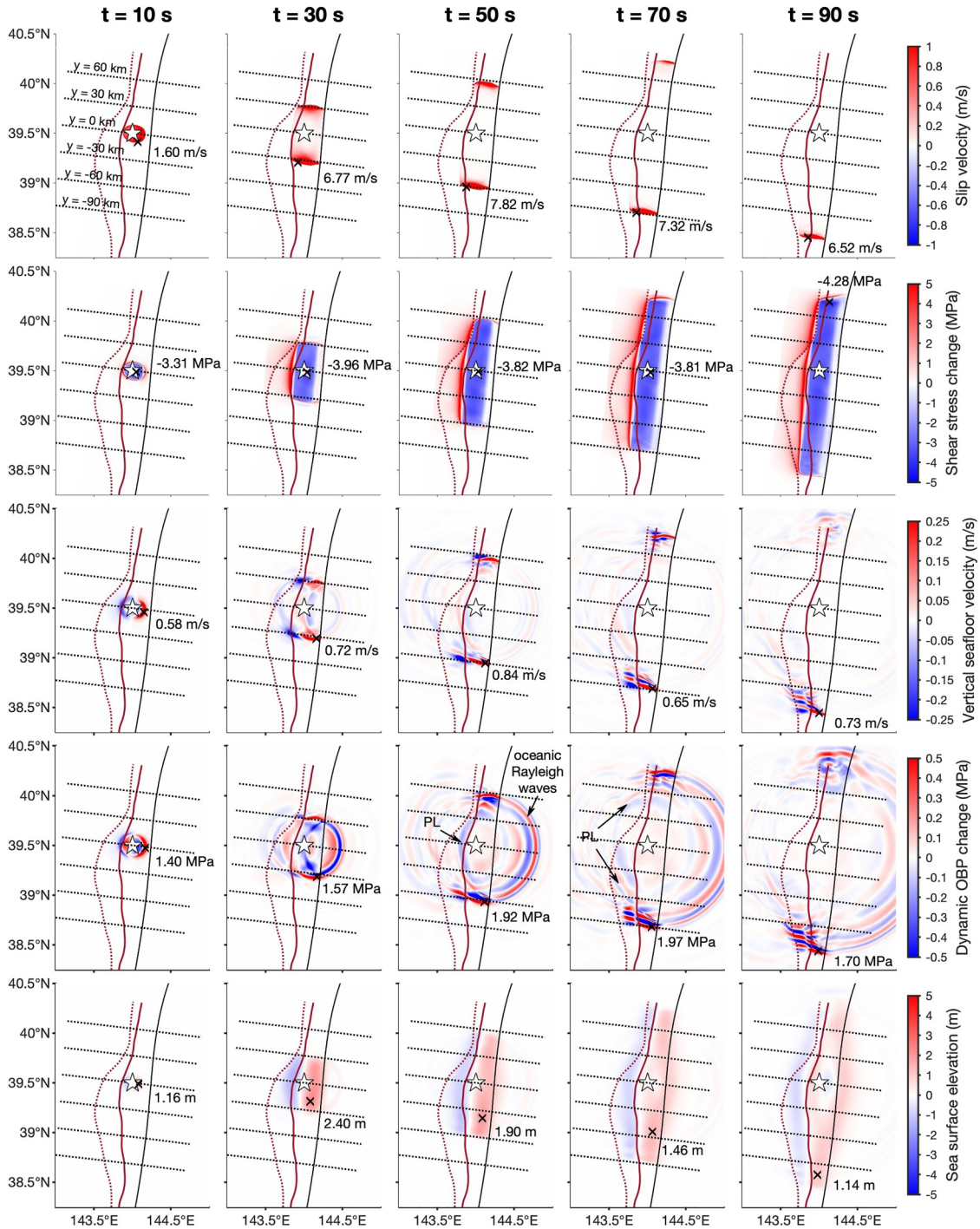

Figure 3. Snapshots of slip velocity, shear stress change, vertical seafloor velocity, dynamic ocean pressure change, and sea surface elevation of the elastic model are shown. Strong ocean acoustic waves are radiated from the rupture fronts in both directions along strike. Large energy is trapped in the sediment behind the rupture fronts, which is the source of radiation. PL and oceanic Rayleigh waves are generated by the updip rupture hitting the trench and rupture fronts propagating along strike. The white star denotes the epicenter. The peak amplitude and location (marked by a symbol ×) are shown in each panel.

of $\sigma_{y'x'}$, thus moving the material away from failure. The inelastic deformation is not seen at depth. The shallow inelastic deformation is due to yielding caused by other stress components in mixed-mode rupture. The rupture front to the south instead increases the amplitude of $\sigma_{y'x'}$ to promote inelastic deformation at depth, leading to slower rupture propagation, smaller slip velocity, and weaker radiation. This asymmetry in rupture speed is

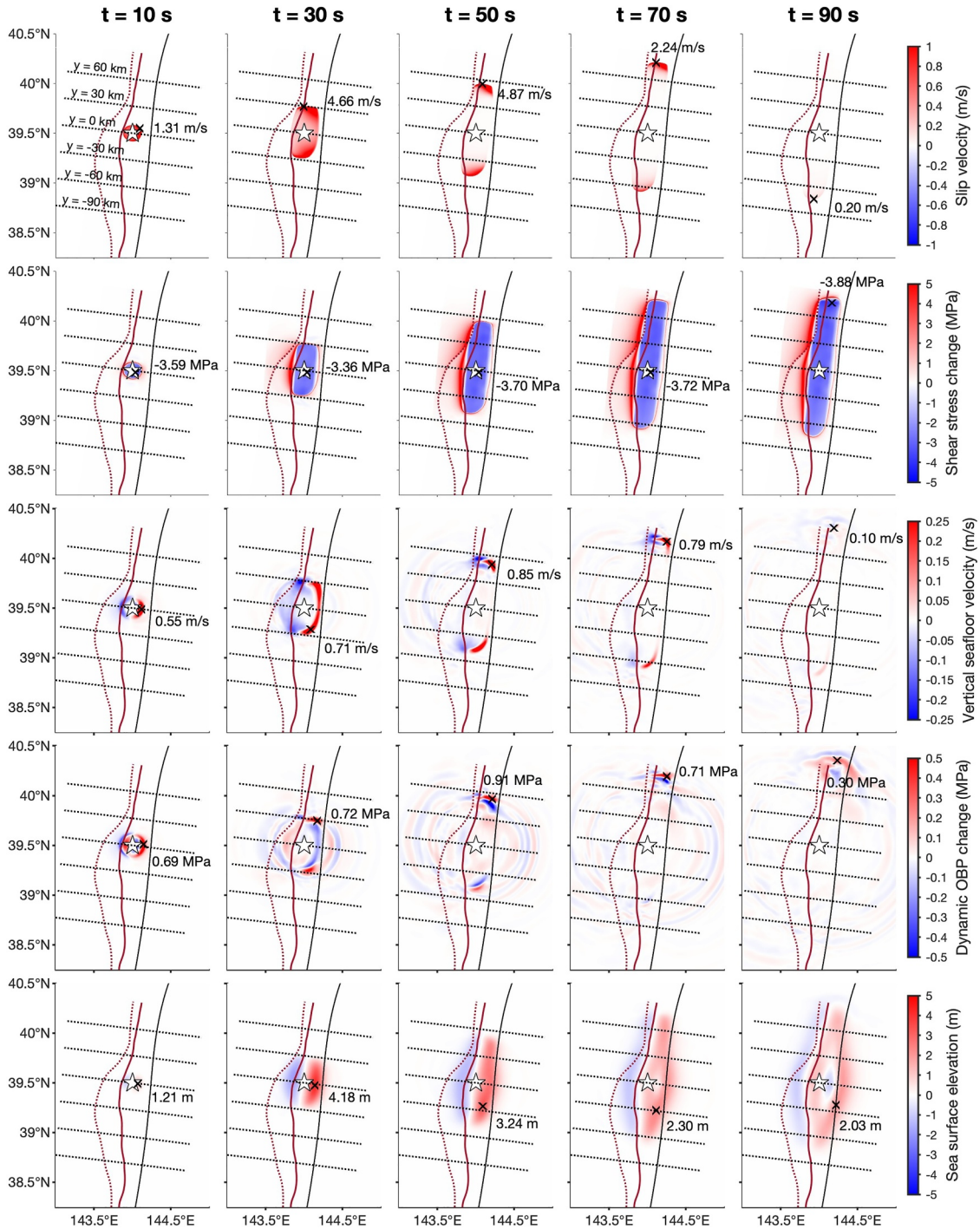

Figure 4. Same as Figure 3 except for the inelastic model. A larger tsunami is produced than that in the elastic model with significantly weaker radiation.

therefore not seen in the elastic model because the off-fault shear stress $\sigma_{y'x'}$ does not affect rupture propagation in an elastic setting.

Figure 5 compares the seafloor displacements at five cross sections between the two models at 300 s. Significant seafloor uplift is caused by inelastic wedge deformation, several times larger than the uplift in the elastic model. The difference between the inelastic wedge deformation in the north and south is also clearly seen. The inelastic zone to the south is wider than the north and peak uplift is in the north, indicating more intense and localized

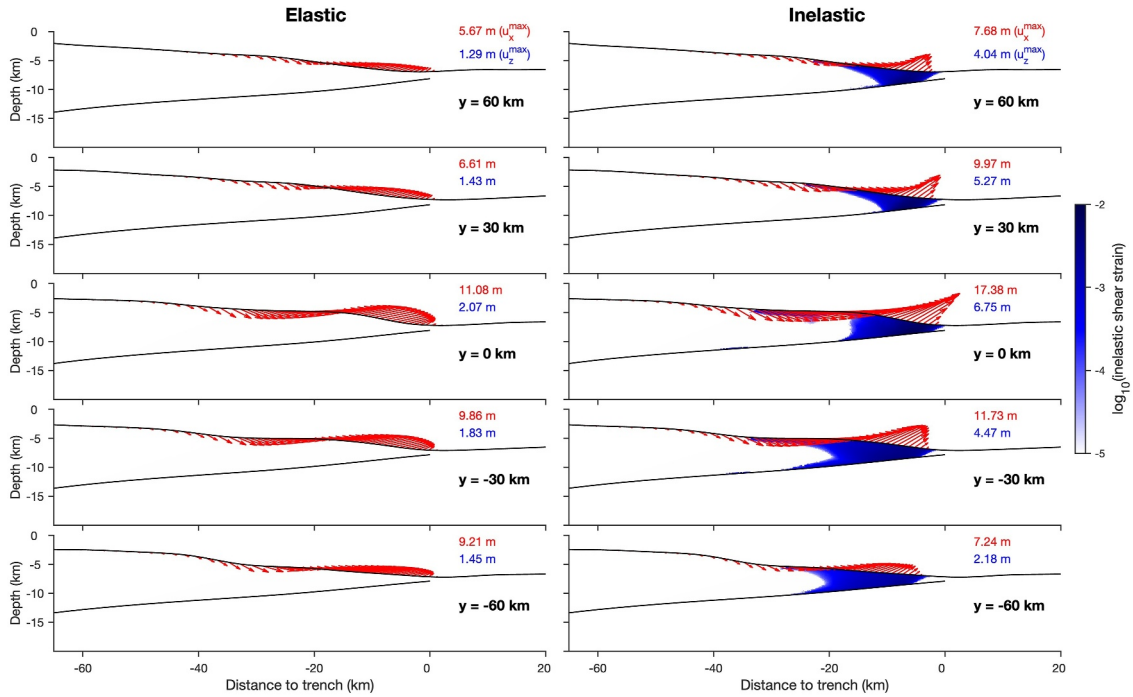

Figure 5. Seafloor displacement and inelastic shear strain at $t = 300$ s are shown at five cross sections (denoted in Figures 3 and 4) for the elastic and inelastic models. Peak horizontal and vertical displacements at each cross section are shown in red and blue numbers, respectively. Significantly larger uplift is generated in the inelastic model. The inelastic shear strain in the wedge, equivalent to volume density of seismic potency, is shown in a logarithmic scale.

inelastic deformation in the north, which is likely driven by the fast rupture velocity at depth. The yielding in the south causes broader inelastic deformation, which slows down the rupture at depth, but the uplift is smaller.

We compare the slip and horizontal and vertical seafloor displacements between the two models at 300 s in Figure 6. The peak slip in the inelastic model is surprisingly larger than the elastic model and there seems to be a large slip patch stretching in all directions from the hypocenter leading to larger horizontal displacement. The peak uplift is more than three times larger in the inelastic model. The width of the seafloor uplift in the inelastic model is significantly narrower than the elastic model. The narrower inelastic zone in the north leads to narrower uplift than in the south. The rupture length in the elastic model is ~200 km controlled by the prescribed frictional parameter $a - b$ (Figure 2), while it is ~180 km in the inelastic model. The shorter rupture length in the inelastic model is due to the rupture dying out by yielding controlled by the off-fault stress $\sigma_{y'x'}$ in the south. No yielding occurs at depth to the north, so the rupture propagates all the way to the prescribed velocity-strengthening region, as in the elastic model. From the rupture time contours we can see that the rupture velocity to the south (<1 km/s) is smaller than to the north (~1.2 km/s) in the inelastic model. The rupture velocity to the north is identical to the rupture velocity in both directions in the elastic model, largely controlled by the S-wave speed of the sediment (1.5 km/s).

Figure S2 in Supporting Information S1 shows the results when we change the shallow velocity-strengthening region to velocity-weakening. Peak slip changes only slightly from 16.93 to 18.35 m in the elastic model. Peak uplift increases slightly from 2.10 to 2.23 m. In the inelastic model, rupture slows down before reaching about $y = -90$ km and then accelerates and reaches about the same extent as in the elastic model, that is, the southward rupture propagates farther than in the velocity-strengthening case. The peak slip increases from 22.12 to 25.64 m; however, the peak uplift reduces from 6.75 to 6.56 m, indicating higher efficiency of generating seafloor uplift by inelastic deformation in the velocity-strengthening region. The rupture velocity pattern is largely similar to Figure 6 for the two velocity-strengthening cases.

To find out why the peak slip in the inelastic model is larger, we show the space-time plots of slip velocity and shear stress change along $y = 0$ as well as relevant time histories at a node closest to the hypocenter (Figure 7). Although the shallow velocity-strengthening zone is present the rupture propagates up dip with a nearly constant

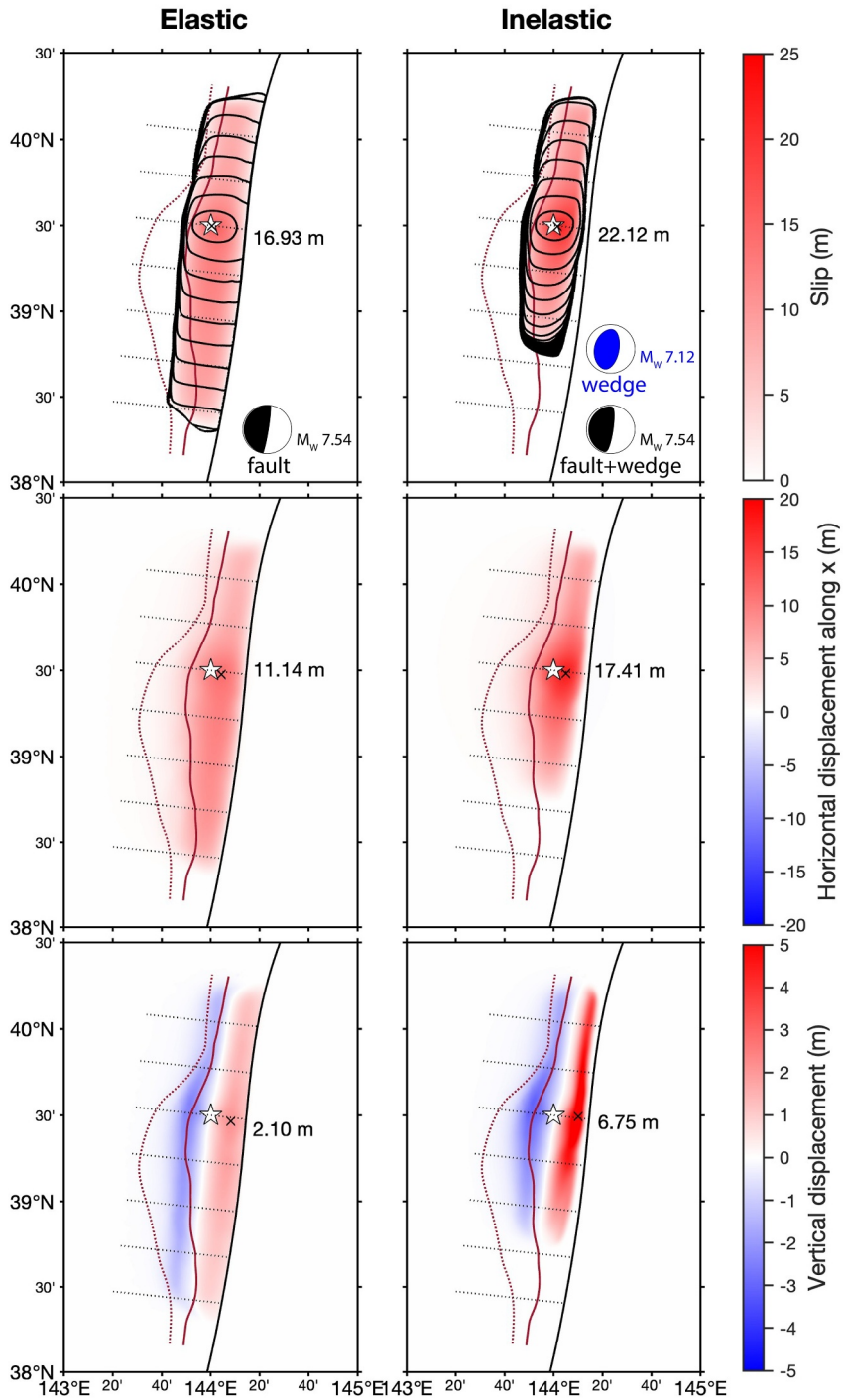

Figure 6. Distributions of slip and horizontal and vertical seafloor displacements are compared between elastic and inelastic models. Rupture time contours every 10 s are shown in the top two panels. The peak amplitude and location (denoted by a symbol ×) are indicated in each panel. The black beachballs in the first row show the focal mechanisms of two models, which includes fault slip in the elastic model and fault slip plus inelastic wedge deformation in the inelastic model, both representing a shallowly dipping thrust earthquake. The seismic moment due to inelastic deformation in the wedge, however, shows a high-angle reverse faulting focal mechanism (blue beachball), indicating a high efficiency of generating uplift. The moment magnitude associated with each beachball is indicated. The peak uplift in the inelastic model is more than 3 times larger than in the elastic model. The larger peak slip in the inelastic model around the hypocenter is due to an increase in slip duration by inelastic deformation shown in Figure 7. In the inelastic model the rupture velocity to the south is slower than to the north and the uplift is wider but smaller in the south.

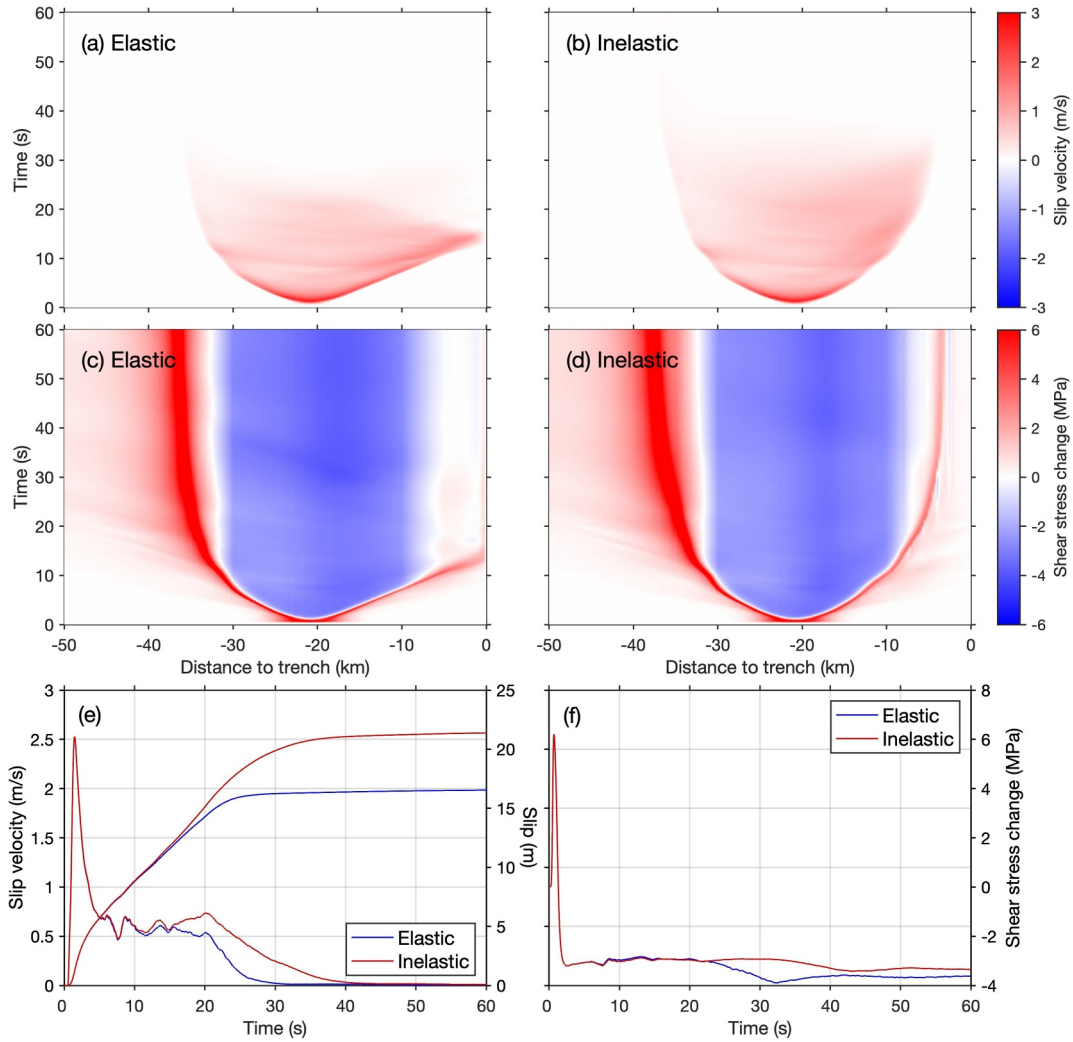

Figure 7. Space-time plots of slip velocity (a, b) and shear stress change (c, d) are compared at $y = 0$ between elastic and inelastic models. Time histories of slip velocity and slip (e) and shear stress change (f) at the closest node to the hypocenter in the finite-element mesh are shown. Longer duration of slip can be clearly seen in (b) than in (a), as well as in (e). The shallow velocity-strengthening region increases shear stress, promoting inelastic deformation in the wedge, and causes slow rupture propagation, increasing slip duration at shallow depths. The longer slip duration at depth in (e) is due to more gradual stress change caused by inelastic deformation, resulting in larger slip in the inelastic model.

sub-Rayleigh rupture velocity in the elastic model, due to strong effects of free surface and bimaterial interface unclamping the fault (Ma & Beroza, 2008). Little reflection is generated at the trench due to the frictional increase in the velocity-strengthening region. The slowing of deep rupture into the velocity-strengthening region is clearly seen. However, in the inelastic model, a very slow rupture propagation up dip is clearly seen, due to inelastic wedge deformation (Figure 5), enhanced by shear stress increase above the velocity-strengthening region. The pronounced longer duration of slip velocity up dip from the hypocenter and plastic dissipation in the inelastic model (Figure 7b) lead to little high-frequency radiation.

The longer slip duration is also seen at the hypocenter in the inelastic model (Figure 7e). Due to a shallow hypocentral depth and large CF used in the model, inelastic wedge deformation occurs up dip from the hypocenter shortly after nucleation (see Movie S2). The inelastic deformation causes more gradual shear stress reduction (Figure 7f), giving rise to ∼10 s longer slip duration at the hypocenter, which leads to larger slip in the inelastic model. The same mechanism occurs in a large patch around the hypocenter, which explains the larger slip pattern shown in Figure 6. This is similar to the >100 m slip patch at shallow depth with modest inelastic deformation for the 2011 Tohoku-Oki earthquake, presented in Ma and Du (2025). Here the inelastic deformation around the

hypocenter is modest due to large confining pressure although the CF is large, so the peak slip rate remains identical to the elastic case and peak slip increases because of longer duration. With significant inelastic deformation, peak slip rate is reduced, and slip is diminished despite longer duration, as seen at shallower depths (Figures 5–7). In Ma and Du (2025), the modest inelasticity near the large slip patch is due to a smaller CF, inelastic deformation occurs near the trench due to large dynamic stress change and low confining pressure. The dilation of seafloor by ocean acoustic waves (see Figure 6 of Ma & Du, 2025) also contributes to the longer slip duration, but here this dilational effect is very small due to a large depth (~10 km).

The seismic potency of the elastic model is 5.1350×10^{10} m^3. The total seismic potency of the inelastic model is 5.1364×10^{10} m^3, with a ratio of seismic potency in the wedge to the fault 0.2953 (the inelastic strain shown in Figure 5 is the volume density of seismic potency). Assuming a shear modulus 5.06 GPa of wedge sediment in the model, the moment magnitude for both models is M_W 7.54. In the inelastic model the moment release in the wedge alone corresponds to M_W 7.12, in contrast to M_W 7.47 due to fault slip. Due to the ambiguity of seismic moment on a bimaterial plate interface in the models (e.g., Ampuero & Dahlen, 2005; Heaton & Heaton, 1989), if we use 20 GPa for the shear modulus the moment magnitudes for both models are M_W 7.94, close to the moment magnitude of the 1896 earthquake. Standard approaches, such as CMT solutions, determine moment magnitude without considering material properties in the source region, which may overestimate the magnitudes of shallow subduction earthquakes (e.g., Polet & Kanamori, 2000).

If we sum all the moment sources in the wedge (using a shear modulus of 5.06 GPa), the moment tensor components $(M_{xx}, M_{yy}, M_{zz}, M_{xy}, M_{xz}, M_{yz})$ for a point source approximation due to inelastic deformation are $(-4.06, -0.49, 4.55, 0.56, 2.01, 0.00) \times 10^{19}$ Nm in the coordinate system shown in Figure 1. Because we do not include inelastic volumetric strain in the model the moment tensor is purely deviatoric. The beachball is plotted in Figure 6, showing a high-angle reverse faulting focal mechanism (the plunge of T axis is 77.36°), as expected from horizontal compression and vertical extension of inelastic deformation, which clearly indicates high efficiency in tsunami generation. The three principal values of the moment tensor are $(-4.58, -0.42, 5.00) \times 10^{20}$ Nm, with a small non-double-couple component ($\varepsilon = -\frac{0.42}{5.00} = -8.4\%$). The actual shape of the beachball and the efficiency of generating inelastic uplift depend on the ratios and the orientations of the initial principal stresses and dynamic stresses during plastic flow. Ma (2022) discussed the importance of the orientation of the minimum principal stress in tsunami generation. The non-double-couple component of the moment tensor can be increased, for example, to obtain a compensated linear vector dipole (CLVD), by setting the initial intermediate and minimum principal stresses in the model approximately equal.

The different radiation characteristics between the elastic and inelastic models are also illustrated in the space-time plots of vertical seafloor velocity and dynamic ocean bottom pressure change (Figure 8). The PL waves generated from updip rupture hitting the trench and by rupture fronts propagating along strike are marked. The large waves trailing behind the rupture front and strong oceanic Rayleigh waves are clearly seen in the elastic model. However, all these features are nearly absent in the inelastic model, consistent with Figures 3 and 4. The radiation to the south is much weaker than to the north in the inelastic model, reflecting the difference in yielding at depth. The radiation from deep rupture to the north in the inelastic model is similar to that in the elastic model. The yellow strips in vertical seafloor velocity at shallow depths in the inelastic model reflect slow and long rupture propagation caused by inelastic deformation as shown in Figure 7b. The yellow strips are shorter to the north of the hypocenter because inelastic deformation is more limited to shallow depths (Figure 5). Little radiation can be seen from yellow strips in both directions in the inelastic model, distinctly different from the elastic model. Similar features can also be seen from the dynamic ocean bottom pressure changes associated with the rupture front.

Figure 9 shows the space-time plots of sea surface elevation at five cross sections between the two models. Clearly larger tsunami in the inelastic model is seen. Ocean acoustic waves are also present. As in Ma and Du (2025), we define the efficiency of tsunami generation as the sea surface elevation normalized by average slip along each cross section. Because the average slip is larger around the hypocenter in the inelastic model the efficiency of tsunami generation is slightly reduced at $y = 0$. However, the larger efficiency in the inelastic model is clearly seen at all the cross sections. Again, this is due to frictional sliding on conjugate Coulomb microfractures with steeper dips than that of the plate interface, shown by the high-angle reverse faulting mechanism of inelastic wedge deformation (Figure 6).

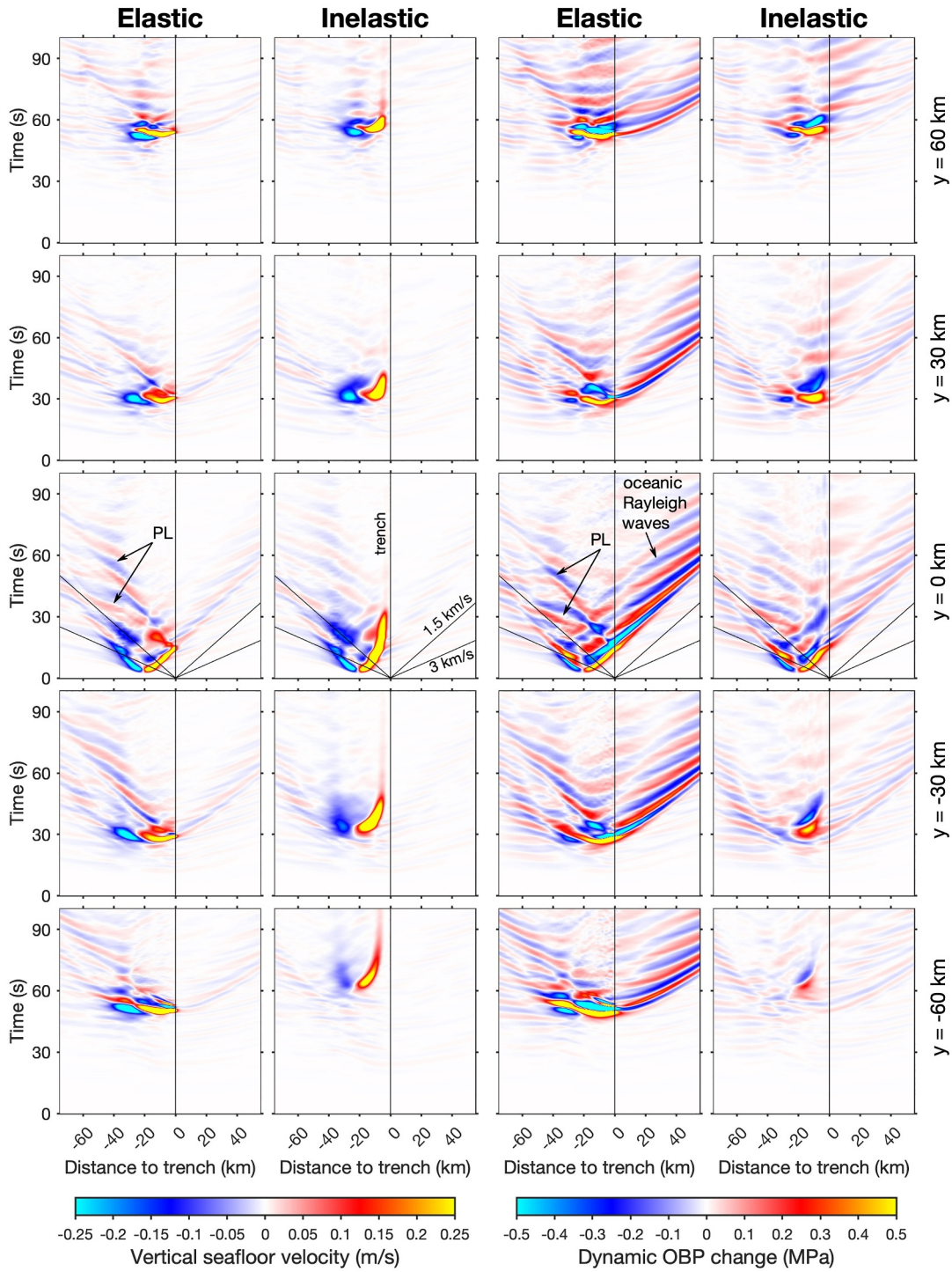

Figure 8. Space-time plots of vertical seafloor velocity and dynamic ocean bottom pressure change at five cross sections are compared between elastic and inelastic models. Stronger PL and oceanic Rayleigh waves are radiated from the rupture front in the elastic model (see also Figures 3 and 4). Little radiation is seen from the rupture front in the inelastic model. In the inelastic model, radiation at the rupture front is weaker to the south of the hypocenter than to the north due to inelastic deformation at depth. The color is saturated. The slopes of straight lines correspond to the P and S wave speeds of wedge sediment.

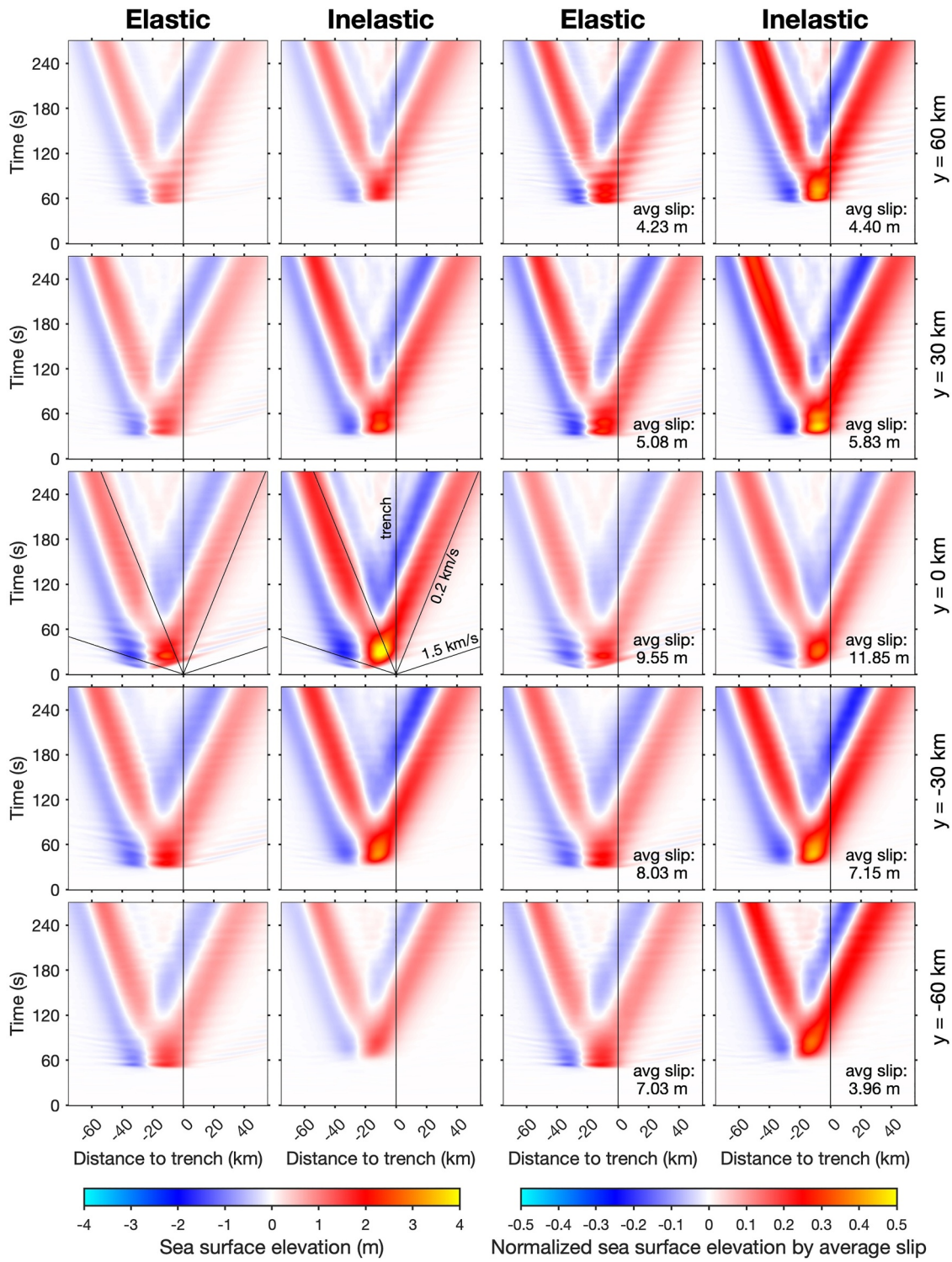

Figure 9. Space-time plots of sea surface elevation and normalized sea surface elevation by average slip are compared between elastic and inelastic models. A larger tsunami and higher efficiency of tsunami generation are observed in the inelastic model.

Figures 10–12 detail the waveforms of vertical seafloor velocity, dynamic ocean bottom pressure change, and sea surface elevation at the five cross sections. Again, the strong radiation of ocean acoustic waves in the elastic model and weak radiation in the inelastic model are clearly shown. However, the tsunami in the inelastic model is

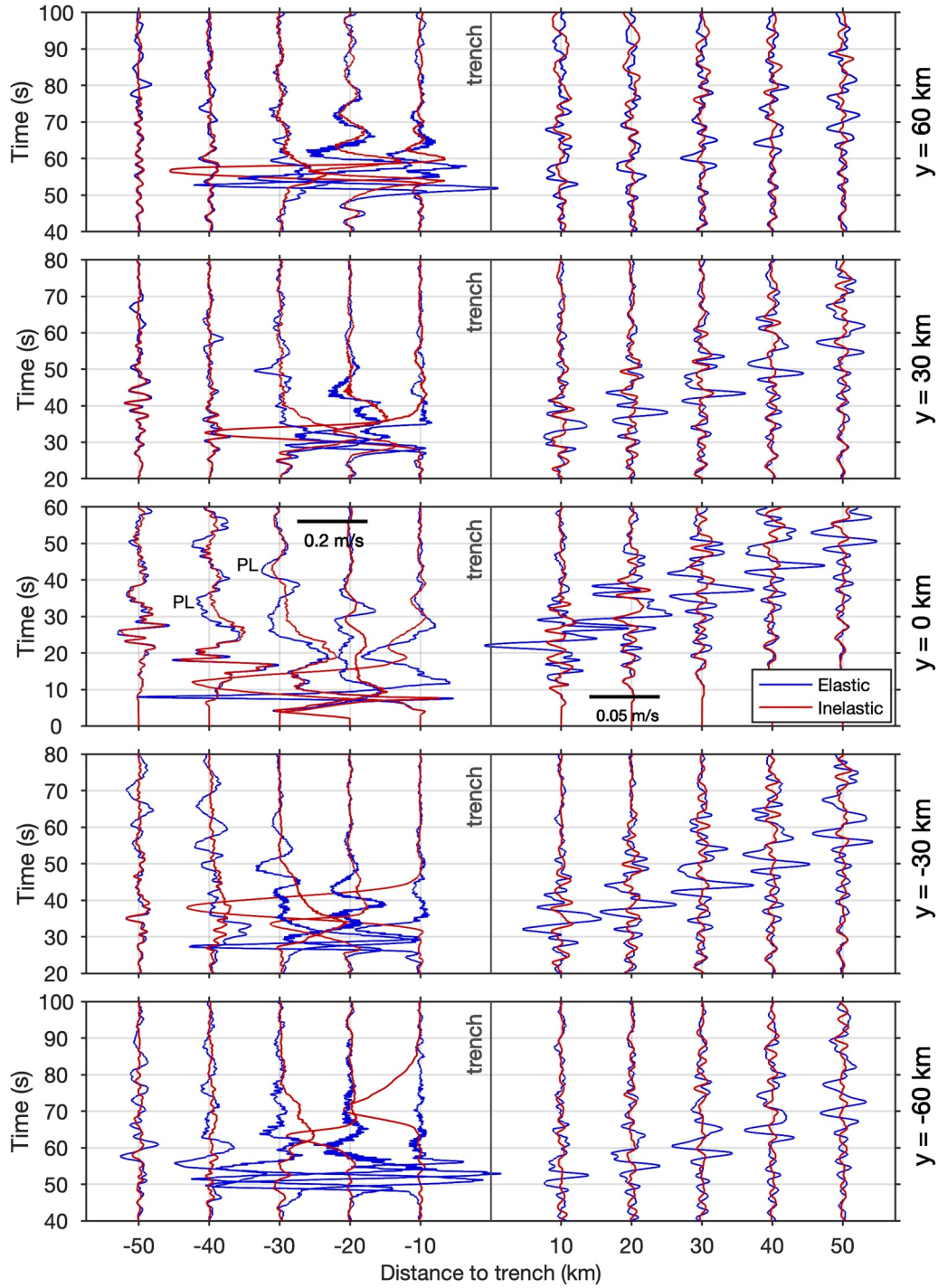

Figure 10. Time histories of vertical seafloor velocities are compared between elastic and inelastic models. Stronger radiation is seen in the elastic model. Large long-duration seafloor velocities are seen in the inelastic model, reflecting slow motion due to enhanced inelastic deformation by the velocity-strengthening friction on the shallow plate interface, but are associated with little radiation. The duration of velocity pulses is longer to the south of the hypocenter due to the role of off-fault shear stress $\sigma_{y'x'}$ in increasing inelastic deformation at depth. PL waves radiated from the up-dip rupture hitting the trench and trapped energy behind the rupture fronts along strike are marked.

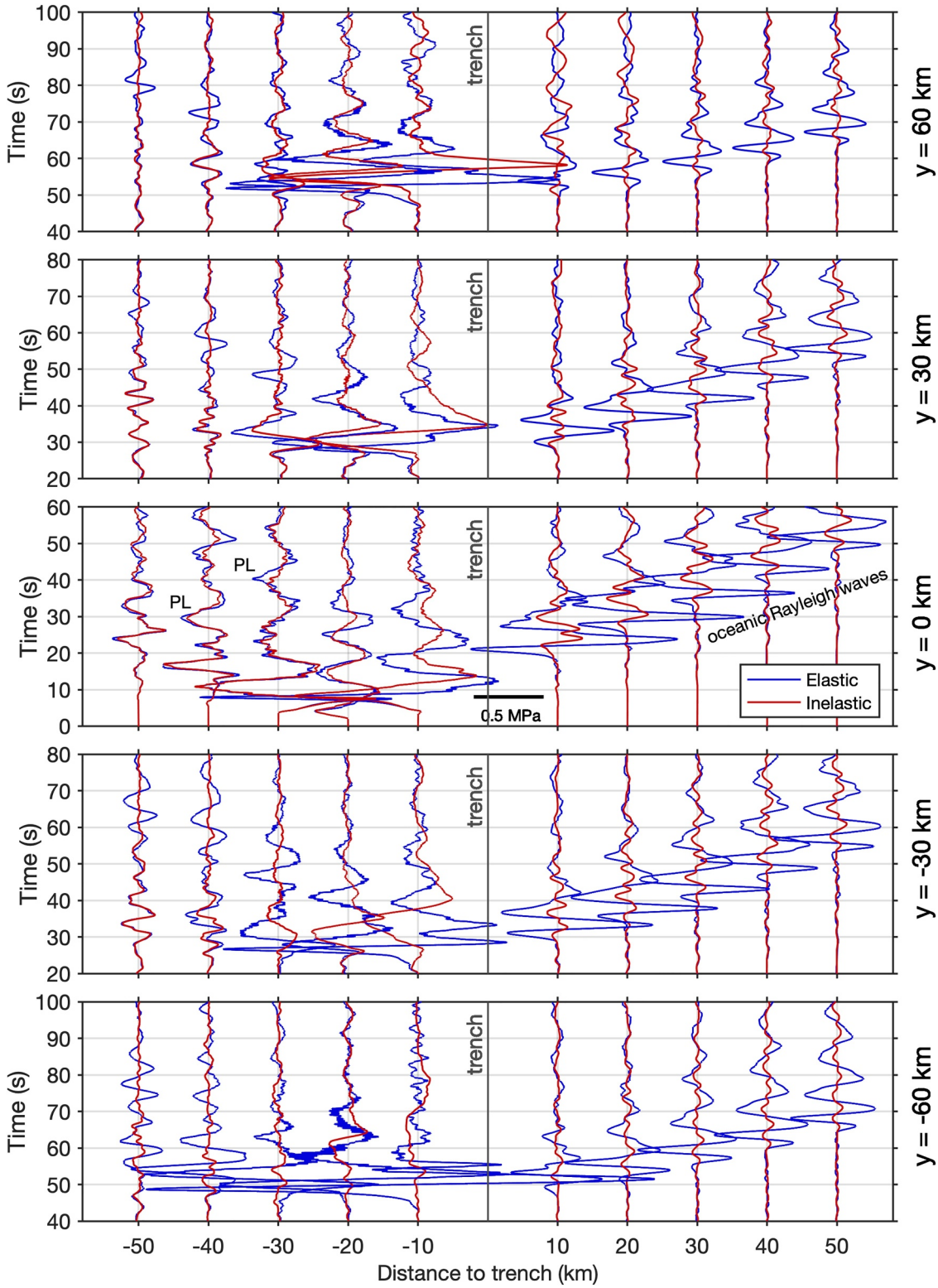

Figure 11. Same as Figure 10 except for dynamic ocean bottom pressure change.

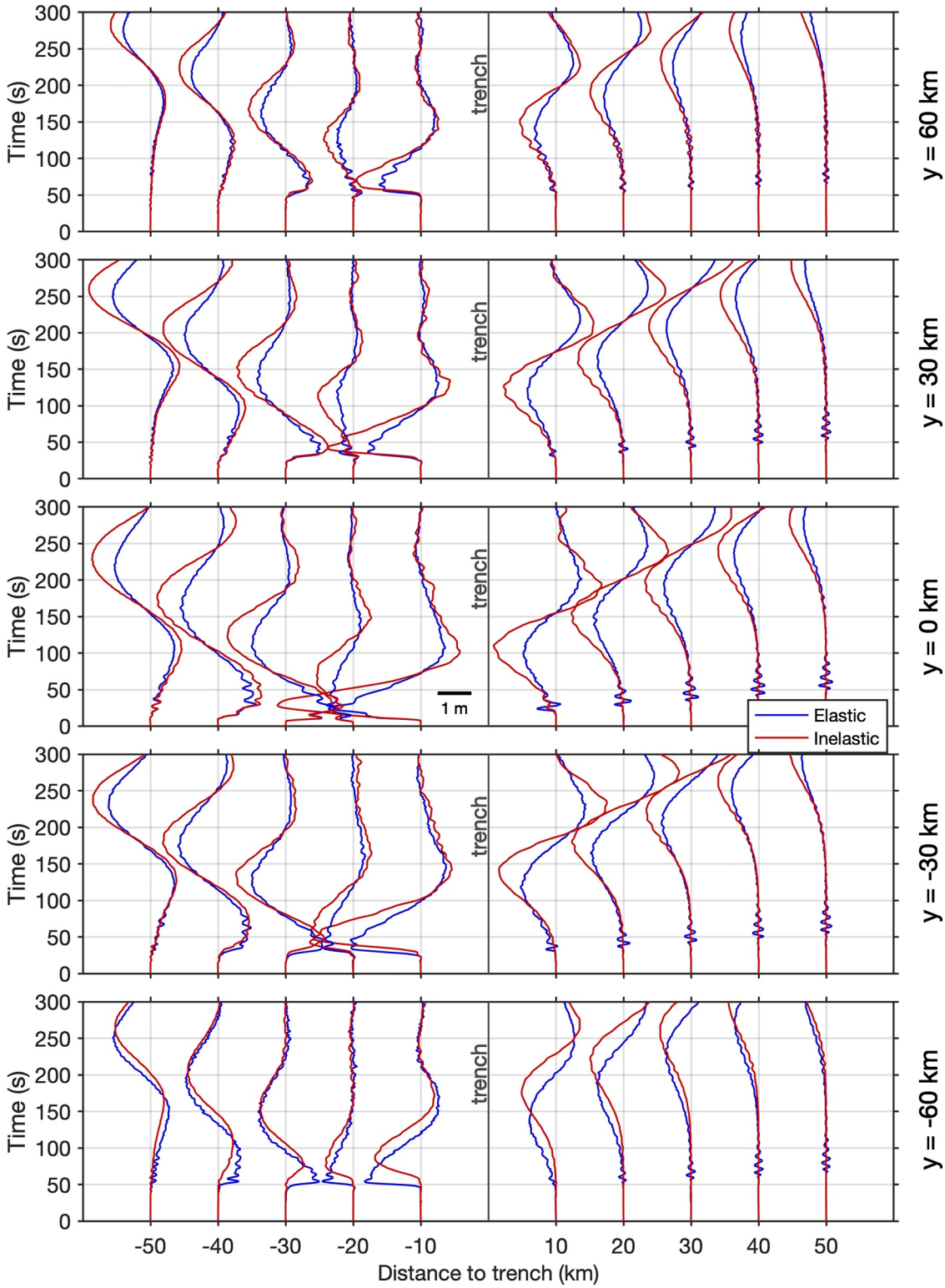

Figure 12. Same as Figure 10 except for sea surface elevation. A larger tsunami is seen in the inelastic model. Short-period ocean acoustic waves are superimposed on the long-period tsunami, showing weaker acoustic radiation in the inelastic model.

significantly larger. We see large and long-duration vertical seafloor velocity at 10 km from the trench, which leads to large seafloor uplift (after time integration). These long-duration velocity pulses correspond to the yellow strips in Figure 8. The duration of pulses is ∼10 s to the north of the hypocenter and is longer to the south; the duration reaches ∼25 s at $y = -60$ km, reflecting the slower rupture propagation to the south. The long-duration velocity pulses are also shown on the horizontal seafloor velocity (Figures S3 and S4 in Supporting Information S1).

Due to the uncertainty in the hypocentral location of the 1896 Sanriku earthquake we also run two additional inelastic rupture scenarios with different hypocenters. One has the hypocenter located at (0, −60 km) and the other with hypocenter at (0, 60 km). All the other rupture parameters remain the same. Movies S3 and S4 show the details of these rupture scenarios. Both ruptures have a longer duration due to predominantly unilateral rupture propagation (Figure 13). For the northern hypocenter the southward rupture is particularly slow. The rupture slows down significantly between $y = 0$ and $y = 30$ km, then continues southward with a very slow rupture velocity (<1 km/s), making the total duration over 200 s. When the hypocenter is in the south the rupture propagates northward faster (∼1.2 km/s). These are again due to the role of off-fault shear stress $\sigma_{y'x'}$ in the yielding for mode III rupture. Yielding only occurs at depth for southward rupture, limiting rupture velocity, slip velocity, rupture propagation distance, and radiation. The inelastic deformation occurs mostly at shallow depth for northward rupture, resulting in a narrower inelastic seafloor uplift and larger peak uplift (7.04 m). The point-source moment tensor in the wedge due to inelastic deformation in both models again show a high-angle reverse faulting mechanism. The moment tensor components $(M_{xx}, M_{yy}, M_{zz}, M_{xy}, M_{xz}, M_{yz})$ are $(-4.39,\ -0.35, 4.73,\ -0.27, 2.03,\ -0.11) \times 10^{19}$ Nm (the plunge of T axis is 77.82°) for the southern hypocenter model and $(-3.57,\ -0.52, 4.10, 0.93, 1.87, 0.06) \times 10^{19}$ Nm (the plunge of T axis is 76.31°) for the northern hypocenter model. The potency ratio between the wedge and fault is 0.2683 (southern hypocenter) and 0.3 (northern hypocenter) for these two models. Both ruptures have weak radiation from the trench due to significant inelastic wedge deformation, but the radiation for the southward rupture (northern hypocenter) is significantly weaker than the northward rupture (southern hypocenter), as seen mostly in energy trapped behind the rupture front (Figure 14 and Movies S3 and S4). Although the tsunami is larger for the northward rupture the efficiency of tsunami generation is similar between the two ruptures (Figure 15). Movies S5 and S6 and Figure S5 in Supporting Information S1 show the results of the elastic models for these two scenarios. The rupture velocity is nearly constant and radiates strong acoustic waves from the rupture front in both along-strike directions. The peak uplift is more than 2–3 times smaller than that of the inelastic models.

We show the potency rate functions for both elastic and inelastic models and all three hypocenter locations (Figure 16). The potency rate time functions within the wedge are also shown for the inelastic models. Inelastic models tend to have longer durations due to slower rupture velocity. When the hypocenter is in the center the duration for the inelastic model is shorter; this is because the longer rupture propagation distance in the elastic model (Figure 6). Despite different rupture velocity and very different radiation characteristics between elastic and inelastic models the potency rate functions are all smooth and have similar spectral decays, which is different from the result in Ma and Hirakawa (2013) because the models here do not have strong rupture breakout at trench due to the shallow velocity-strengthening region and buried ruptures. All the models are shallow subduction events. A larger difference between deep rupture and shallow rupture may exist, as shown by Lay et al. (2012) and Ma and Hirakawa (2013). On the other hand, the results here show that the potency (or moment) rate time function may not well represent the radiation characteristics of earthquakes because rupture complexities can be canceled out by a point source approximation.

Inelastic wedge deformation contributes to seismic potency (moment), however, is a large energy sink due to plastic dissipation (Ma & Hirakawa, 2013). Ma and Hirakawa (2013) derived the general energy balance equations for inelastic deformation. We calculate the radiated energy for each rupture scenario based on equations 1, 2, 4, and 5 in Ma and Hirakawa (2013) and the results are shown in Table 1. In the calculation, we use the models by excluding the ocean (treating seafloor as a free surface) because the slowly propagating tsunami affects the motion of the solid earth after a long time. The rupture dynamics for the models without ocean are, however, nearly identical to the models with ocean. The less radiated energy in the inelastic models than in the elastic models is clearly seen. The shear modulus of 5.06 MPa of wedge sediment is used to calculate the moment. The moment-scaled radiated energy for three elastic models is similar to typical crustal earthquakes, such as the 2004 Parkfield earthquake (Ma et al., 2008). A larger shear modulus would make the moment-scaled radiated energy lower. More importantly, the moment-scaled radiated energy for the elastic model is 6.28, 5.29, and 11.20 times

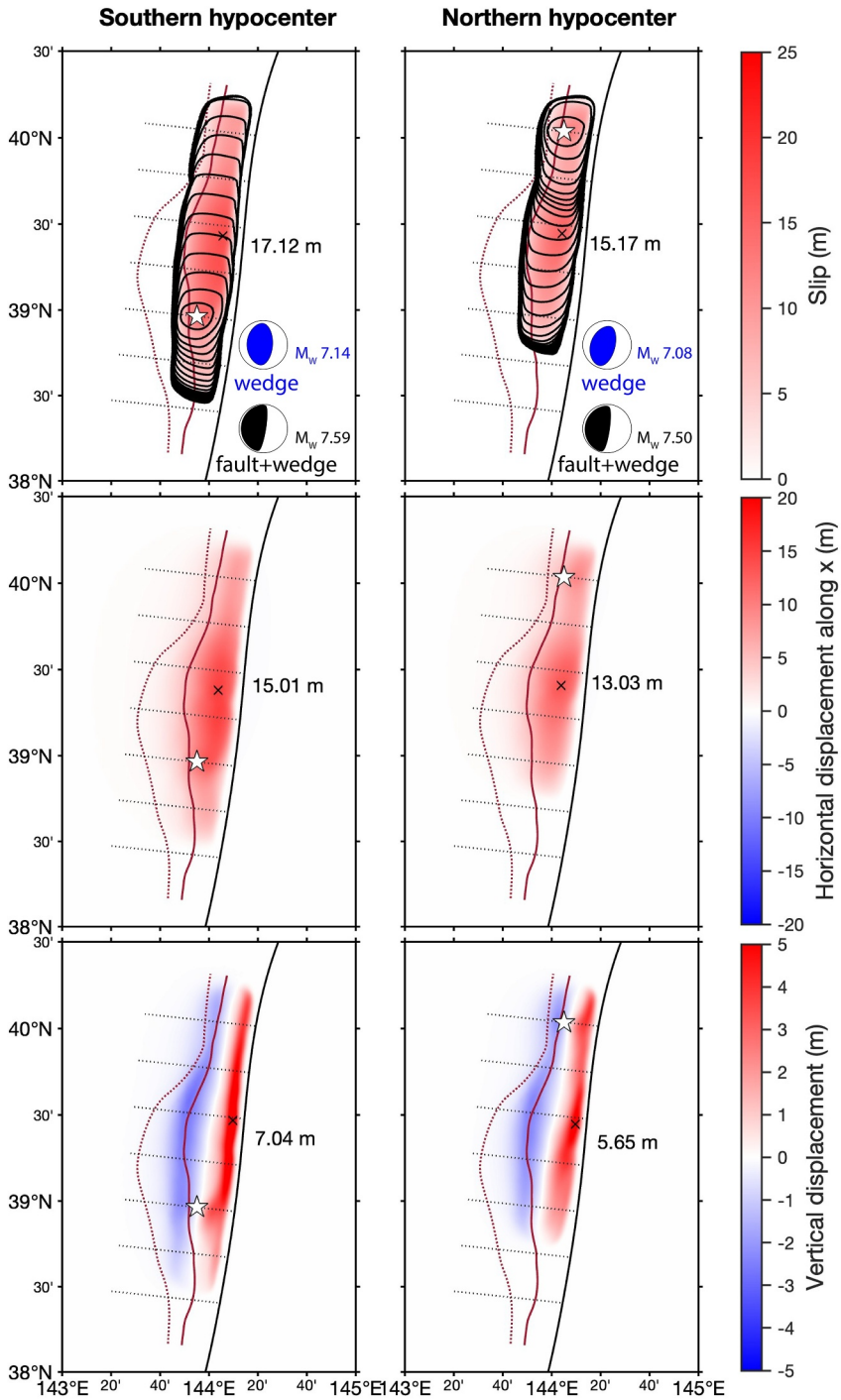

Figure 13. Distributions of slip, rupture time contours (every 10 s), and horizontal and vertical seafloor displacements are compared for ruptures with inelastic wedge deformation and different hypocenter locations (marked by white stars). The beachball solutions and their moment magnitudes are shown in the lower right corner of the top two panels. The high-angle reverse faulting focal mechanism of inelastic wedge deformation is a manifestation of high efficiency in generating seafloor uplift. The peak amplitude and location in each panel are shown. The rupture velocity to the south is slower than that to the north in both models due to the role of off-fault shear stress $\sigma_{y'x'}$ in controlling the inelastic deformation for mode III rupture at depth.

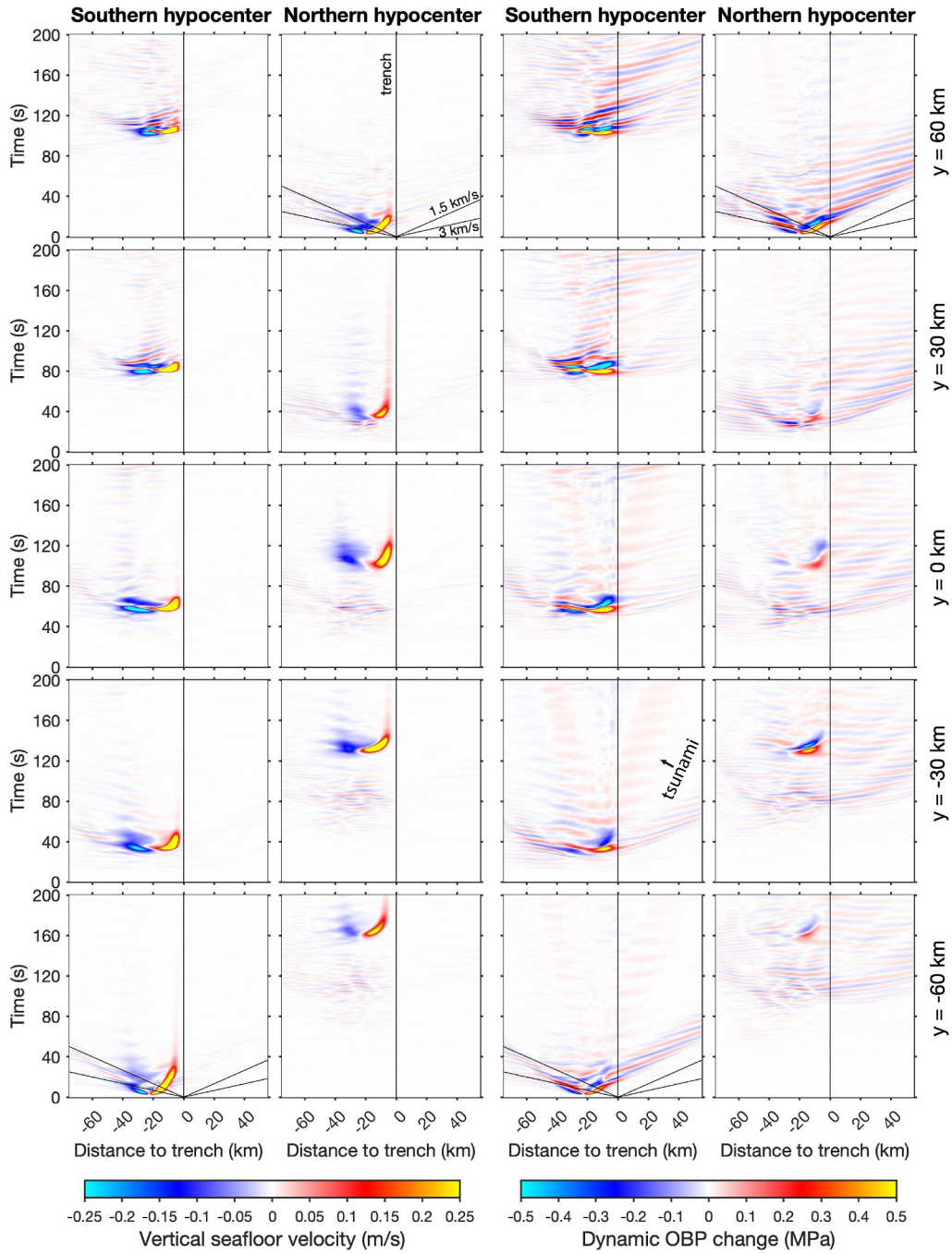

Figure 14. Space-time plots of vertical seafloor velocity and dynamic ocean bottom pressure change at five cross sections are compared between the inelastic models with northern and southern hypocenters. Stronger radiation to the north for a southern hypocenter than to the south for a northern hypocenter is seen. The yellow strip at the rupture front in vertical velocity represents slow deformation (the color is saturated) and is shorter to the north and longer to the south, due to the effect of off-fault shear stress $\sigma_{y'x'}$ on inelastic deformation. The slowly-propagating tsunami can be seen in the right two columns.

larger than that of inelastic model for all the 3 cases (central, southern, and northern hypocenters), respectively, irrespective of shear modulus being used, which is consistent with the observations of tsunami earthquakes (Lay et al., 2012; Newman & Okal, 1998). Inelastic deformation thus provides an explanation for this anomalous characteristic of tsunami earthquakes, suggested by Ma and Hirakawa (2013).

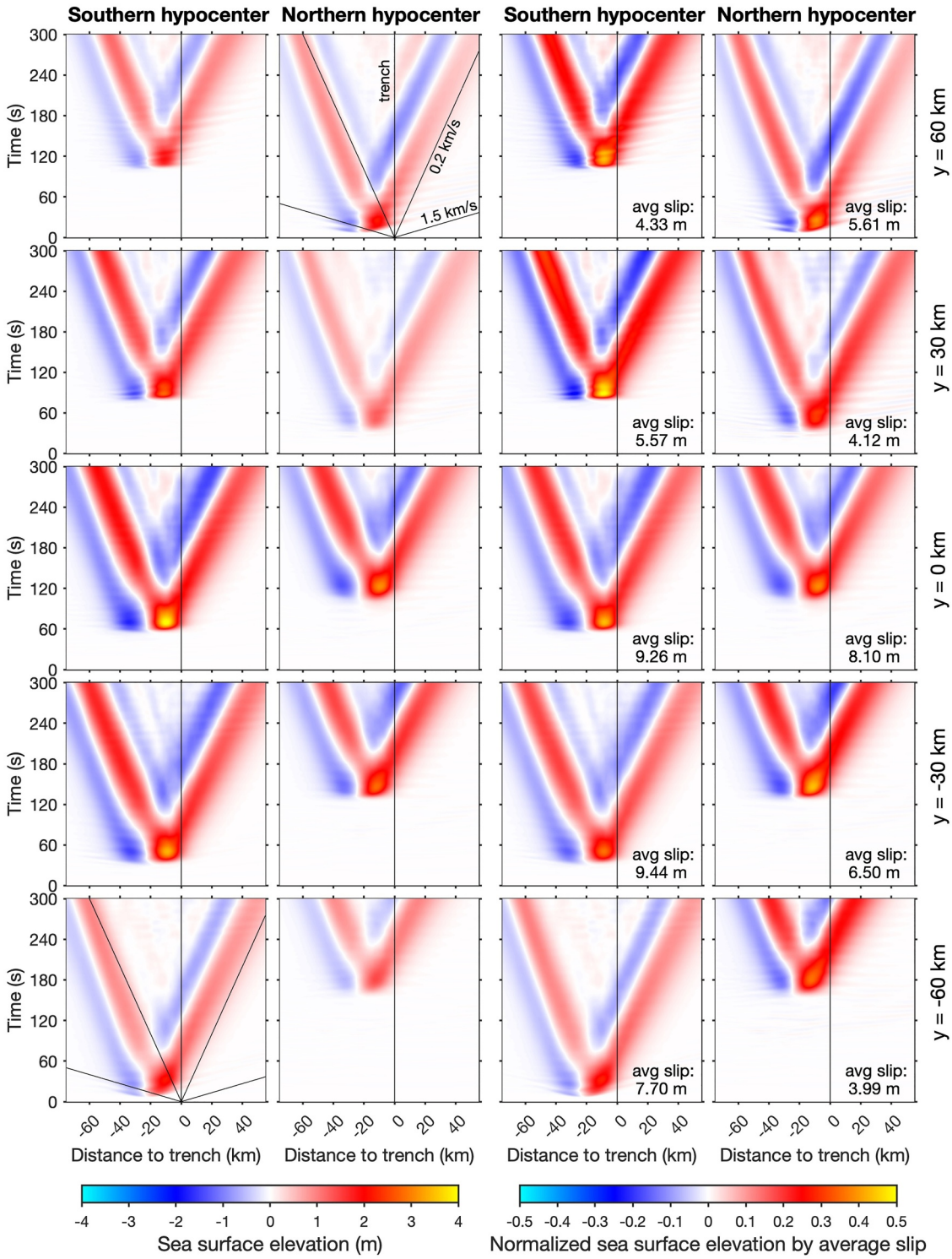

Figure 15. Space-time plots of unnormalized and normalized sea surface elevation by average slip at five cross sections are compared between the inelastic models with northern and southern hypocenters. Northward rupture produces a larger tsunami, but the efficiency of tsunami generation is similar between the two models.

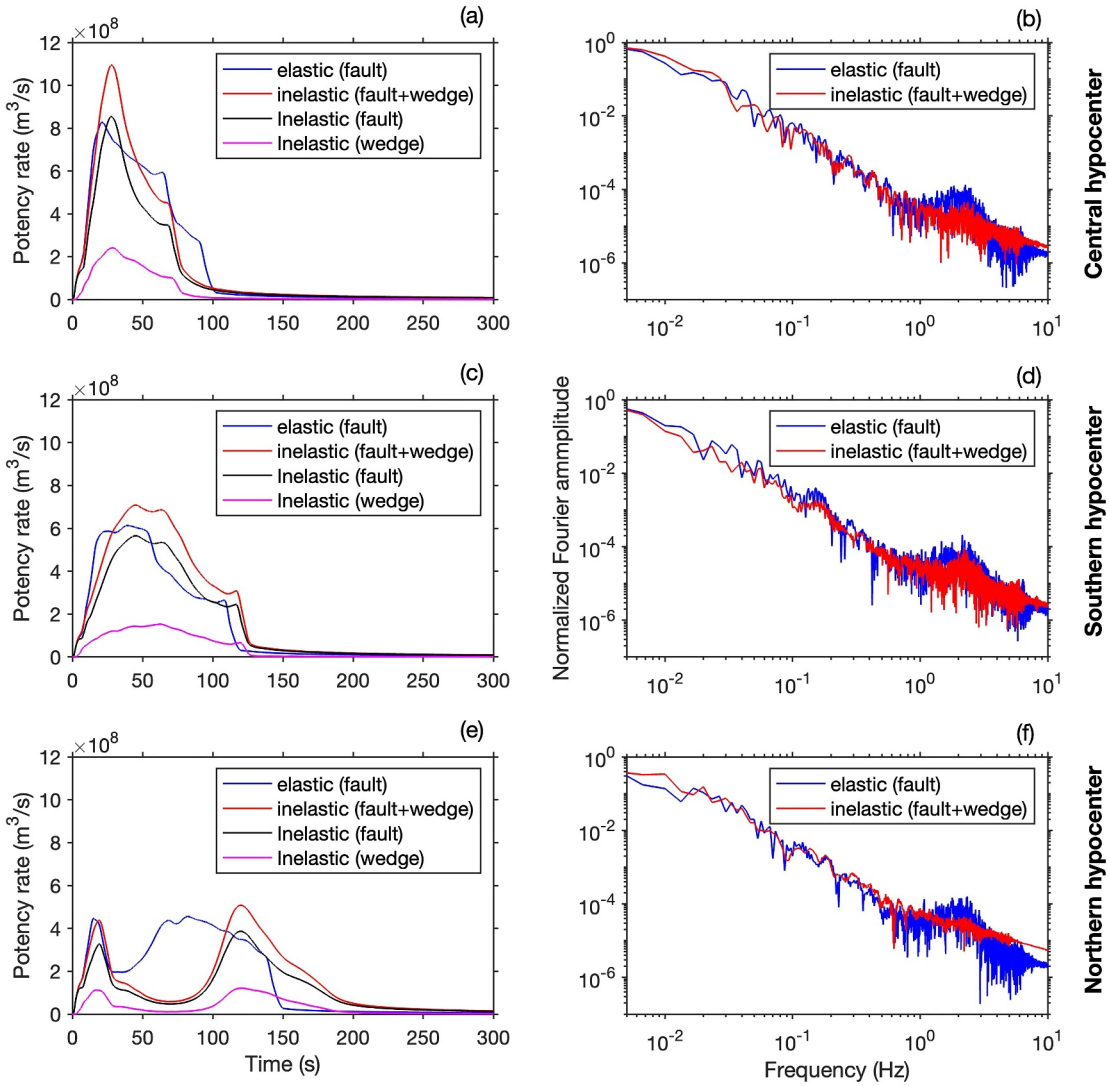

Figure 16. Potency rate time functions and spectra for the elastic and inelastic models with three different hypocenter locations are compared: central hypocenter (a, b), southern hypocenter (c, d), and northern hypocenter (e, f). The potency rate functions in the wedge in the inelastic models are also shown. Inelastic models tend to produce longer rupture durations than elastic models due to a slower rupture velocity. The spectra of these potency rate functions, however, are similar due to their overall smoothness.

Table 1
Seismic Potency, Moment, Radiated Energy, and Energy-to-Moment Ratio for Six Rupture Models

	Central hypocenter		Southern hypocenter		Northern hypocenter	
	Elastic	Inelastic	Elastic	Inelastic	Elastic	Inelastic
Potency (m^3)	5.14×10^{11}	5.17×10^{11}	4.76×10^{11}	6.08×10^{11}	4.87×10^{11}	4.46×10^{11}
Moment (Nm)	2.60×10^{20}	2.62×10^{20}	2.41×10^{20}	3.08×10^{20}	2.47×10^{20}	2.26×10^{20}
Radiated energy (J)	3.13×10^{15}	5.04×10^{14}	2.77×10^{15}	6.70×10^{14}	3.39×10^{15}	2.77×10^{14}
E_R/M_0	1.21×10^{-5}	1.93×10^{-6}	1.15×10^{-5}	2.17×10^{-6}	1.38×10^{-5}	1.23×10^{-6}

4. Discussion

We have presented fully coupled models of dynamic rupture, ocean acoustic waves, and tsunami for the 1896 Sanriku earthquake. The models do not represent the detailed rupture process of the earthquake due to limited observations available; instead they emphasize the physics of inelastic deformation in explaining the anomalous characteristics of this earthquake. Realistic bathymetry, fault geometry and velocity structure from the JIVSM, and along-strike variation of sediment thickness in the Japan Trench are incorporated. The modeled rupture zone is within 40 km from the trench and below thick sediment in the northern Japan Trench, which is shown to have significant effects on rupture dynamics, seismic and acoustic radiations, and tsunami generation. Although sediment has long been realized to play an important role in the deficiency in high-frequency radiation of tsunami earthquakes due to its low rigidity (e.g., Lay et al., 2012; Polet & Kanamori, 2000; Sallarès & Ranero, 2019) our models show that sediment in an elastic setting leads to strong high-frequency radiation, contradicting the observations.

The weak strength of sediment has largely been overlooked in the community. Our models show that inelastic deformation can occur in the sedimentary overriding wedge due to weak strength, which acts as a large energy sink and causes slow rupture propagation, deficiency in high-frequency radiation, and low moment-scaled energy. Nearly all the seismic and ocean acoustic radiations (mostly PL and oceanic Rayleigh waves) are strongly diminished by inelastic deformation. Little radiation is observed from the rupture front. The moment-scaled energy of inelastic models can be an order of magnitude lower than that of elastic models. Meanwhile frictional sliding on conjugate Coulomb microfractures (represented by inelastic deformation) generates seafloor uplift more efficiently than slip on a shallowly dipping plate interface, reflected in high-angle reverse faulting focal mechanisms of seismic moment due to inelastic wedge deformation. Our models with velocity-strengthening friction at shallow depth show that inelastic wedge deformation enhanced by shear stress increase on the fault causes seafloor uplift 2–3 times larger than purely elastic models. Carvajal et al. (2022) showed that buried ruptures at shallow depth are more efficient in generating seafloor uplift than trench-breaking ruptures in their 2D elastic dislocation models. However, the higher efficiency of tsunami generation by inelastic deformation than by buried ruptures is clearly shown in the models here. Inelastic deformation in the overriding wedge due to weak sediment thus provides a possible unifying interpretation to nearly all the anomalous characteristics of the 1896 Sanriku earthquake and is likely applicable to other tsunami earthquakes, which may challenge the widely used elastic dislocation models (e.g., Cheung et al., 2021; Felix et al., 2021; Lay et al., 2012; Sallarès & Ranero, 2019; Satake et al., 2017; Yue et al., 2014). The large inelastic uplift shown in Figures 6 and 13 can be misinterpreted as large shallow slip or submarine landslides, as tsunami data have little sensitivity to the physics of tsunami generation. However, the moment sources due to inelastic wedge deformation shown in this work produce additional radiation that can be used to differentiate different mechanisms for tsunami generation.

The 1896 Sanriku earthquake, like most other tsunami earthquakes, propagated mainly along strike, which is a predominantly mode III rupture. We have shown that the anti-plane off-fault shear stress $\sigma_{y'x'}$ (y' is along strike and x' along dip) plays an important role in controlling yielding in mode III ruptures. This stress component is reduced by northward rupture but increased by southward rupture, given the oblique plate convergence and stress setting in the northern Japan Trench. Thus, yielding occurs mostly to the south of the hypocenter at depth. The limit on this stress component placed by yielding reduces rupture velocity and radiation to the south. Meanwhile, the northward rupture prevents yielding at depth, so rupture velocity is mostly controlled by the S wave of the sediment. In both rupture directions yielding occurs at shallow depth due to stresses in mixed rupture modes. However, the inelastic zone to the north is narrower than the south. This finding should not be confused with the slow northward rupture propagation (~850 m/s) in the northern Japan Trench in the 2011 Tohoku-Oki earthquake models of Ma (2023) and Ma and Du (2025). The inelastic deformation in those models is caused by the rupture deeper than the sedimentary wedge and large dynamic stresses ahead of the rupture front driven by the rupture breakout at trench to the south. Heterogeneous stress and fault friction along strike (e.g., Bilek & Lay, 2002) and horst-and-graben structure (e.g., Polet & Kanamori, 2000) can also play an important role in rupture velocity and radiation, which should be included in future models. The differences in radiation between elastic and inelastic models are likely more pronounced if future models are pushed to include higher frequencies.

Due to weak high-frequency radiation of ocean acoustic waves (e.g., PL waves) their use for tsunami early warning (e.g., Kozdon & Dunham, 2014; Lay et al., 2019) is cautioned, which was pointed out in Wilson and Ma (2021) and Ma and Du (2025). These high-frequency waves are valuable in locating earthquakes and

estimating magnitudes, but probably carry little information about tsunami, which has much longer periods and is more sensitive to static deformation (see Figure 12). Okal et al. (2003) presented a similar counter-argument for the use of T waves for tsunami early warning.

5. Conclusions

We conclude our study with the following points:

- The two essential characteristics of the 1896 Sanriku earthquake (large tsunamigenesis and depletion in high-frequency radiation) are explained by the inelastic deformation of thick wedge sediment in the northern Japan Trench without large near-trench slip. Inelastic wedge deformation also explains slow rupture velocity and ~10 times lower moment-scaled radiated energy, thus accounting for nearly all the anomalous characteristics of this tsunami earthquake.
- Inelastic wedge deformation is shown to represent a reverse faulting focal mechanism with a steep plunge of T axis (>75°), reflecting high efficiency in generating seafloor uplift. The additional radiation from this source, if observed, can be used to test different hypotheses for tsunami generation (i.e., shallow slip, submarine landslide, or inelastic wedge deformation). Moment tensors due to inelastic deformation in the wedge can be included as unknowns (in addition to fault slip) in future kinematic source inversions by using elastic Green's functions; this combined source can probably better model tsunami generation and depletion in high-frequency radiation in an elastic setting.
- Shallow velocity-strengthening region enhances shear stress and promotes dynamic failure of weak wedge sediment, leading to more efficient tsunamigenesis than large shallow or buried slip, and meanwhile causes depletion in high-frequency radiation.
- Anti-plane off-fault shear stress can play an important role in the inelastic deformation and rupture speed along strike in tsunami earthquakes.
- Ocean acoustic waves, such as PL and oceanic Rayleigh waves, are strongly weakened by inelastic wedge deformation, which may not produce robust tsunami early warning signals.
- Long-duration ground velocity pulses can naturally result from inelastic off-fault deformation.

Conflict of Interest

The authors declare no conflicts of interest relevant to this study.

Data Availability Statement

The source codes and input files to produce the models in this work are available via Zenodo (Du & Ma, 2025).

Acknowledgments
We thank Eric Dunham, two anonymous reviewers, and Steve Day for insightful comments that greatly improved the paper and Tatsuya Kubota and Tatsuhiko Saito for stimulating discussions. This work was supported by the National Science Foundation (award no. EAR-2244703).

References

Abe, K. (1978). A dislocation model of the 1933 Sanriku earthquake consistent with the tsunami waves. *Journal of Physics of the Earth*, *26*(4), 381–396. https://doi.org/10.4294/jpe1952.26.381

Ampuero, J.-P., & Dahlen, F. A. (2005). Ambiguity of the moment tensor. *Bulletin of the Seismological Society of America*, *95*(2), 390–400. https://doi.org/10.1785/0120040103

Andrews, D. J. (1976). Rupture propagation with finite stress in antiplane strain. *Journal of Geophysical Research*, *81*(20), 3575–3582. https://doi.org/10.1029/jb081i020p03575

Andrews, D. J. (2004). Rupture models with dynamically determined breakdown displacement. *Bulletin of the Seismological Society of America*, *94*(3), 769–775. https://doi.org/10.1785/0120030142

Andrews, D. J. (2005). Rupture dynamics with energy loss outside the slip zone. *Journal of Geophysical Research*, *110*(B1), B01307. https://doi.org/10.1029/2004JB003191

Bilek, S. L., & Lay, T. (2002). Tsunami earthquakes possibly widespread manifestations of frictional conditional stability. *Geophysical Research Letters*, *29*(14). https://doi.org/10.1029/2002gl015215

Carvajal, M., Sun, T., Wang, K., Luo, H., & Zhu, Y. (2022). Evaluating the tsunamigenic potential of buried versus trench-breaching megathrust slip. *Journal of Geophysical Research: Solid Earth*, *127*(8), e2021JB023722. https://doi.org/10.1029/2021jb023722

Cheung, K. F., Lay, T., Sun, L., & Yamazaki, Y. (2021). Tsunami size variability with rupture depth. *Nature Geoscience*, *15*(1), 33–36. https://doi.org/10.1038/s41561-021-00869-z

Dahlen, F. A. (1984). Noncohesive critical Coulomb wedges: An exact solution. *Journal of Geophysical Research*, *89*(B12), 10125–10133. https://doi.org/10.1029/jb089ib12p10125

Drucker, D. C., & Prager, W. (1952). Soil mechanics and plastic analysis or limit design. *Quarterly of Applied Mathematics*, *10*(2), 157–165. https://doi.org/10.1090/qam/48291

Du, Y., & Ma, S. (2025). Wedge inelasticity and fully coupled models of dynamic rupture, ocean acoustic waves, and tsunami in the Japan Trench: 1896 Sanriku earthquake [Software and input]. *Zenodo*. https://doi.org/10.5281/zenodo.15832304

Du, Y., Ma, S., Kubota, T., & Saito, T. (2021). Impulsive tsunami and large runup along the Sanriku coast of Japan produced by an inelastic wedge deformation model. *Journal of Geophysical Research: Solid Earth*, *126*(8), e2021JB022098. https://doi.org/10.1029/2021jb022098

Felix, R. P., Hubbard, J. A., Moore, J. D. P., & Switzer, A. D. (2021). The role of frontal thrusts in tsunami earthquake generation. *Bulletin of the Seismological Society of America*, *112*(2), 680–694. https://doi.org/10.1785/0120210154

Fujiwara, T. (2021). Seafloor geodesy from repeated multibeam bathymetric surveys: Application to seafloor displacement caused by the 2011 Tohoku-Oki earthquake. *Frontiers in Earth Science*, *9*, 667666. https://doi.org/10.3389/feart.2021.667666

Fujiwara, T., dos Santos Ferreira, C., Bachmann, A. K., Strasser, M., Wefer, G., Sun, T., et al. (2017). Seafloor displacement after the 2011 Tohoku-Oki earthquake in the Northern Japan Trench examined by repeated bathymetric surveys. *Geophysical Research Letters*, *44*(23). https://doi.org/10.1002/2017gl075839

Heaton, T. H., & Heaton, R. E. (1989). Static deformations from point forces and force couples located in welded elastic Poissonian halfspaces: Implications for seismic moment tensors. *Bulletin of the Seismological Society of America*, *79*, 813–841.

Hirakawa, E., & Ma, S. (2016). Dynamic fault weakening and strengthening by gouge compaction and dilatancy in a fluid-saturated fault zone. *Journal of Geophysical Research: Solid Earth*, *121*(8), 5988–6008. https://doi.org/10.1002/2015JB012509

Iki, T. (1897). Field survey report of the 1896 Sanriku tsunami. Rep Imp Earthq Invest Comm (Vol. *11*, pp. 5–34).

Kanamori, H. (1972). Mechanism of tsunami earthquakes. *Physics of the Earth and Planetary Interiors*, *6*(5), 346–359. https://doi.org/10.1016/0031-9201(72)90058-1

Kanamori, H., & Kikuchi, M. (1993). The 1992 Nicaragua earthquake: A slow tsunami earthquake associated with subducted sediments. *Nature*, *361*(6414), 714–716. https://doi.org/10.1038/361714a0

Kodaira, S., Linuma, T., & Imai, K. (2021). Investigating a tsunamigenic megathrust earthquake in the Japan Trench. *Science*, *371*(6534), eabe1169. https://doi.org/10.1126/science.abe1169

Kodaira, S., Nakamura, Y., Yamamoto, Y., Obana, K., Fujie, G., No, T., et al. (2017). Depth-varying structural characters in the rupture zone of the 2011 Tohoku-Oki earthquake. *Geosphere*, *13*(5), 1408–1424. https://doi.org/10.1130/ges01489.1

Koketsu, K., Miyake, H., & Suzuki, H. (2012). Japan integrated velocity structure model version 1. In *Proceedings of the 15th World Conference on Earthquake Engineering*. Retrieved from https://www.iitk.ac.in/nicee/wcee/article/WCEE2012_1773.pdf

Kozdon, J. E., & Dunham, E. M. (2014). Constraining shallow slip and tsunami excitation in megathrust ruptures using seismic and ocean acoustic waves recorded on ocean-bottom sensor networks. *Earth and Planetary Science Letters*, *396*, 56–65. https://doi.org/10.1016/j.epsl.2014.04.001

Kubota, T., Saito, T., & Hino, R. (2022). A new mechanical perspective on a shallow megathrust near-trench slip from the high-resolution fault model of the 2011 Tohoku-Oki earthquake. *Progress in Earth and Planetary Science*, *9*(1), 68. https://doi.org/10.1186/s40645-022-00524-0

Kutschera, F., Gabriel, A.-A., & Dunham, E. M. (2025). CRESCENT Tsunami Benchmark (TTPV1 and TTPV2): 3D fully coupled earthquake dynamic rupture and tsunami benchmarks with varying bathymetric complexity. *Zenodo*. https://doi.org/10.5281/zenodo.15389414

Lay, T., Kanamori, H., Ammon, C. J., Koper, K. D., Hutko, A. R., Ye, L., et al. (2012). Depth-varying rupture properties of subduction zone megathrust faults. *Journal of Geophysical Research*, *117*(B4). https://doi.org/10.1029/2011jb009133

Lay, T., Liu, C., & Kanamori, H. (2019). Enhancing tsunami warning using P wave coda. *Journal of Geophysical Research: Solid Earth*, *124*(10), 10583–10609. https://doi.org/10.1029/2019JB018221

Lotto, G. C., & Dunham, E. M. (2015). High-order finite difference modeling of tsunami generation in a compressible ocean from offshore earthquakes. *Computational Geosciences*, *19*(2), 327–340. https://doi.org/10.1007/s10596-015-9472-0

Ma, S. (2012). A self-consistent mechanism for slow dynamic deformation and tsunami generation for earthquakes in the shallow subduction zone. *Geophysical Research Letters*, *39*(11). https://doi.org/10.1029/2012gl051854

Ma, S. (2022). Dynamic off-fault failure and tsunamigenesis at strike-slip restraining bends: Fully-coupled models of dynamic rupture, ocean acoustic waves, and tsunami in a shallow bay. *Tectonophysics*, *838*, 229496. https://doi.org/10.1016/j.tecto.2022.229496

Ma, S. (2023). Wedge plasticity and a minimalist dynamic rupture model for the 2011 M_W 9.1 Tohoku-Oki Earthquake and tsunami. *Tectonophysics*, *869*, 230146. https://doi.org/10.1016/j.tecto.2023.230146

Ma, S., & Beroza, G. C. (2008). Rupture dynamics on a bi-material interface for dipping faults. *Bulletin of the Seismological Society of America*, *98*(4), 1642–1658. https://doi.org/10.1785/0120070201

Ma, S., Custódio, S., Archuleta, R. J., & Liu, P. (2008). Dynamic modeling of the 2004 M_W 6.0 Parkfield, California, earthquake. *Journal of Geophysical Research*, *113*(B2). https://doi.org/10.1029/2007jb005216

Ma, S., & Du, Y. (2025). Wedge inelasticity and fully coupled models of dynamic rupture, ocean acoustic waves, and tsunami in the Japan Trench: The 2011 M_W 9.1 Tohoku-Oki earthquake. *Tectonophysics*, *910*, 230831. https://doi.org/10.1016/j.tecto.2025.230831

Ma, S., & Hirakawa, E. T. (2013). Dynamic wedge failure reveals anomalous energy radiation of shallow subduction earthquakes. *Earth and Planetary Science Letters*, *375*, 113–122. https://doi.org/10.1016/j.epsl.2013.05.016

Ma, S., & Nie, S. (2019). Dynamic wedge failure and along-arc variations of tsunamigenesis in the Japan Trench margin. *Geophysical Research Letters*, *46*(15), 8782–8790. https://doi.org/10.1029/2019gl083148

Matsuo, H. (1933). *Report on the survey of the 1933 Sanriku tsunami* (Vol. 24, pp. 83–136). Rep Civil Eng Lab.

Newman, A. V., & Okal, E. A. (1998). Teleseismic estimates of radiated seismic energy: The *E/m*0 discriminant for tsunami earthquakes. *Journal of Geophysical Research*, *103*(B11), 26885–26898. https://doi.org/10.1029/98jb02236

Okal, E. A., Alasset, P.-J., Hyvernaud, O., & Schindelé, F. (2003). The deficient T waves of tsunami earthquakes. *Geophysical Journal International*, *152*(2), 416–432. https://doi.org/10.1046/j.1365-246x.2003.01853.x

Polet, J., & Kanamori, H. (2000). Shallow subduction zone earthquakes and their tsunamigenic potential. *Geophysical Journal International*, *142*(3), 684–702. https://doi.org/10.1046/j.1365-246x.2000.00205.x

Sallarès, V., & Ranero, C. R. (2019). Upper-plate rigidity determines depth-varying rupture behaviour of megathrust earthquakes. *Nature*, *576*(7785), 96–101. https://doi.org/10.1038/s41586-019-1784-0

Satake, K., Fujii, Y., Harada, T., & Namegaya, Y. (2013). Time and space distribution of coseismic slip of the 2011 Tohoku earthquake as inferred from tsunami waveform data. *Bulletin of the Seismological Society of America*, *103*(2B), 1473–1492. https://doi.org/10.1785/0120120122

Satake, K., Fujii, Y., & Yamaki, S. (2017). Different depths of near-trench slips of the 1896 Sanriku and 2011 Tohoku earthquakes. *Geoscience Letters*, *4*(1), 33. https://doi.org/10.1186/s40562-017-0099-y

Scholz, C. H. (1998). Earthquakes and friction laws. *Nature*, *391*(6662), 37–42. https://doi.org/10.1038/34097

Shuto, N., Imamura, F., Koshimura, S., Satake, K., & Matsutomi, H. (2007). *Encyclopedia of tsunami (Tsunami no Jiten)* (p. 350). Asakura Publishing. Tokyo.

Tanioka, Y., & Satake, K. (1996). Tsunami generation by horizontal displacement of ocean bottom. *Geophysical Research Letters*, *23*(8), 861–864. https://doi.org/10.1029/96gl00736

Tanioka, Y., & Seno, T. (2001). Sediment effect on tsunami generation of the 1896 Sanriku tsunami earthquake. *Geophysical Research Letters*, *28*(17), 3389–3392. https://doi.org/10.1029/2001gl013149

Tsuru, T., Park, J., Miura, S., Kodaira, S., Kido, Y., & Hayashi, T. (2002). Along-arc structural variation of the plate boundary at the Japan Trench Margin: Implication of interplate coupling. *Journal of Geophysical Research*, *107*(B12). https://doi.org/10.1029/2001jb001664

Utsu, T. (1979). *Seismicity of Japan from 1885 through 1925* (Vol. 54, pp. 253–308). Bulletin of Earthquake Research Institute.

Utsu, T. (1994). Aftershock activity of the 1896 Sanriku earthquake. *Zisin*, *47*(1), 89–92. https://doi.org/10.4294/zisin1948.47.1_89

Wilson, A., & Ma, S. (2021). Wedge plasticity and fully coupled simulations of dynamic rupture and tsunami in the Cascadia subduction zone. *Journal of Geophysical Research: Solid Earth*, *126*(7), e2020JB021627. https://doi.org/10.1029/2020jb021627

Yue, H., Lay, T., Rivera, L., Bai, Y., Yamazaki, Y., Cheung, K. F., et al. (2014). Rupture process of the 2010 M_w 7.8 Mentawai tsunami earthquake from joint inversion of near-field hr-GPS and teleseismic body wave recordings constrained by tsunami observations. *Journal of Geophysical Research: Solid Earth*, *119*(7), 5574–5593. https://doi.org/10.1002/2014JB011082